CHEMISTRY
A EUROPEAN JOURNAL

DOI: 10.1002/chem.200601389

Tuning the Polarization Along Linear Polyaromatic Strands for Rationally Inducing Mesomorphism in Lanthanide Nitrate Complexes

Emmanuel Terazzi,[a] Laure Guénée,[a] Pierre-Yves Morgantini,*[b] Gérald Bernardinelli,[c] Bertrand Donnio,[d] Daniel Guillon,[d] and Claude Piguet*[a]

Abstract: The opposite orientation of the ester spacers in the rodlike ligands $\mathbf{L4}^{C12}$ (benzimidazole-OOC-phenyl) and $\mathbf{L5}^{C12}$ (benzimidazole-COO-phenyl) drastically changes the electronic structure of the aromatic systems, without affecting their meridional tricoordination to trivalent lanthanides, Ln^{III}, and their thermotropic liquid crystalline (i.e., mesomorphic) behaviors. However, the rich mesomorphism exhibited by the complexes $[Ln(\mathbf{L4}^{C12})(NO_3)_3]$ (Ln = La–Lu) vanishes in $[Ln(\mathbf{L5}^{C12})(NO_3)_3]$, despite superimposable molecular structures and comparable photophysical properties. Density functional theory (DFT) and time-dependant DFT calculations performed in the gas phase show that the inversion of the ester spacers has considerable effects on the electronic structure and polarization of the aromatic groups along the strands, which control residual intermolecular interactions responsible for the formation of thermotropic liquid-crystalline phases. As a rule of thumb, an alternation of electron-poor and electron-rich aromatic rings favors intermolecular interactions between the rigid cores and consequently mesomorphism, a situation encountered for $\mathbf{L4}^{C12}$, $\mathbf{L5}^{C12}$, $[Ln(\mathbf{L4}^{C12})(NO_3)_3]$, but not for $[Ln(\mathbf{L5}^{C12})(NO_3)_3]$. The intercalation of an additional electron-rich diphenol ring on going from $[Ln(\mathbf{L5}^{C12})(NO_3)_3]$ to $[Ln(\mathbf{L6}^{C12})(NO_3)_3]$ restores mesomorphism despite an unfavorable orientation of the ester spacers, in agreement with our simple predictive model.

Keywords: electrostatic potentials · intermolecular interactions · lanthanides · liquid crystals · metallomesogens

Introduction

According to a chemical point of view, the usual design of thermotropic liquid crystals relies on the preparation of molecules containing two contradictory (i.e., antinomic) parts separated by a molecular interface.[1] The first part corresponds to a polarizable rigid core (often made up of flat polyaromatic systems), to which long and poorly polarizable flexible alkyl, alkoxy, or siloxy chains (i.e. the second part) are connected. For these molecules in the crystalline state, the minimum free energy results from a micro-segregation process, in which the close packing of the rigid core maximizes intermolecular (mainly transient) electrostatic interactions, while the peripheral flexible chains optimally fill the

[a] Dr. E. Terazzi, Dr. L. Guénée, Prof. Dr. C. Piguet
Department of Inorganic, Analytical and Applied Chemistry
University of Geneva, 30 quai E. Ansermet, 1211 Geneva 4 (Switzerland)
Fax: (+41) 22-379-6830
E-mail: Claude.Piguet@chiam.unige.ch

[b] Dr. P.-Y. Morgantini
Department of Physical Chemistry
University of Geneva, 30 quai E. Ansermet, 1211 Geneva 4 (Switzerland)
Fax: (+41) 22-379-3216
E-mail: Pierre-Yves.Morgantini@chiphy.unige.ch

[c] Dr. G. Bernardinelli
Laboratory of X-ray Crystallography
University of Geneva, 24 quai E. Ansermet, 1211 Geneva 4 (Switzerland)

[d] Dr. B. Donnio, Dr. D. Guillon
Institut de Physique et Chimie des Matériaux de Strasbourg-IPCMS
Groupe des Matériaux Organiques
UMR 7504 (CNRS/Université Louis Pasteur)
23 rue du Loess, B.P. 43, 67034 Strasbourg Cedex 2 (France)

Supporting information for this article is available on the WWW under http://www.chemeurj.org/ or from the author. It contains additional tables (Tables S1–S16) and figures (Figure S1–S13) for structural and spectroscopic analyses, and crystallographic data for compounds **2**, $\mathbf{L5}^{Cl}$, $[Eu(\mathbf{2})(NO_3)_3(H_2O)](CH_3NO_2)$ (**17**) and $[Yb(\mathbf{L5}^{C0})(NO_3)_3](CH_3CN)_2$ (**18**) in CIF formats.

interstitial voids.[2] A thermotropic liquid-crystalline phase, often referred to as a thermotropic mesophase, forms upon warming up the crystals to the melting temperature T_m, for which the flexible peripheral chains are molten and adopt a liquidlike behavior. Since the interactions between poorly polarizable chains is weak (i.e. ΔH_m^{chains} is small), but the release of configurational entropy upon melting is considerable for the flexible chains (i.e. ΔS_m^{chains} is large), the melting temperature $T_m \approx \Delta T_m^{chains} = \Delta H_m^{chains}/\Delta S_m^{chains}$ is low. Further heating of the mesophase produces a second phase transition, characterized by the clearing temperature $T_c \approx \Delta T_m^{cores} = \Delta H_m^{cores}/\Delta S_m^{cores}$, at which the rigid polarizable cores are completely decorrelated, and a liquid is formed.[2] Evidently, these successive melting and clearing processes are not strictly decoupled and a partial dissociation of the intermolecular interactions involving the rigid polarizable cores already occurs during the melting process leading to the mesophase. However, the simplistic consideration of a thermotropic mesophase as containing residual polarizable clusters made up of packed rigid aromatic cores dispersed in a continuum of the liquidlike molten flexible chains, helps in correlating microscopic molecular structures and macroscopic thermal behaviors.[2] With this model in mind, the introduction of bulky molecular objects with considerable three-dimensional extension close to the rigid core is harmful for the mesogenic properties, because ΔH_m^{cores} decreases to such an extent that the clearing and melting processes merge, and the liquid-crystalline phase vanishes.[3] The latter effect represents a serious limiting factor for producing metallomesogens, that is, metal-containing liquid crystals, because the bulky metallic unit is usually introduced within the aromatic rigid core.[4] In this context, the trivalent lanthanide cations, Ln^{III}, correspond to an extreme case because their extended coordination spheres are poorly compatible with the specific molecular anisometries required for an efficient packing of the cores.[5] For instance, the mesogenic ligand $\mathbf{L1}^{C12}$ ($Cr \xrightarrow{132\,^\circ C} SmA \xrightarrow{188\,^\circ C} I$) and $\mathbf{L2}^{C12}$ ($Cr \xrightarrow{144\,^\circ C} SmA \xrightarrow{193\,^\circ C} I$) lose their mesomorphism upon complexation of the central tridentate 2,6-bis(benzimidazol-2-yl)pyridine to $Ln(NO_3)_3$.[6]

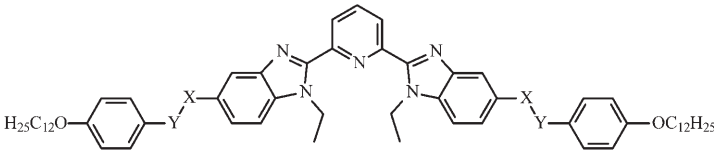

$X = CH_2$, $Y = O$: $\mathbf{L1}^{C12}$ $\quad Cr \xrightarrow{132\,^\circ C} SmA \xrightarrow{188\,^\circ C} I$

$X = O$, $Y = CH_2$: $\mathbf{L2}^{C12}$ $\quad Cr \xrightarrow{144\,^\circ C} SmA \xrightarrow{193\,^\circ C} I$

Among the rare successes obtained in designing lanthanidomesogens, that is, lanthanide-containing mesogens,[2c] three main strategies can be recognized.

1) Ln^{III} or LnX_3 are embedded in a cocoon of wrapped aromatic rings, which ensures a significant enthalpic contribution ΔH_m^{cores} to the clearing process, as found in monodentate Schiff bases[7] and in planar macrocylic phthalocyanines.[8]
2) A large number of diverging flexible chains are attached to the central aromatic binding units in order to give polycatenar ligands with large entropic contributions ΔS_m^{chains}, which produces a melting temperature low enough to promote liquid-crystalline behavior.[9]
3) The rigid aromatic cores responsible for the residual intermolecular cohesion in the mesophase are spatially decoupled from the bulky lanthanide unit, thus preserving ΔH_m^{cores} large enough to give high-temperature clearing processes.[10]

These considerations suggest that ΔS_m^{chains} is currently the only rationally tunable parameter for programming lanthanido mesogens (second strategy), while some concomitant, but empirical control of ΔH_m^{cores} results from the minimization of the pertubation brought by the metallic core (first and third strategies). A fourth unexplored strategy may benefit from recent improvements in the understanding and the modeling of aromatic π–π stacking interactions,[11] which allows some simple electrostatic modeling of the intermolecular packing occurring between rigid aromatic cores in mesophases.[12] A rational tuning of ΔH_m^{cores} may thus result from a judicious exploitation of the two main characteristics of interacting π systems.

1) The dominant interaction in these systems correspond to π-electron repulsion. The introduction of electron-attracting atoms or substituents decreases π–π electron repulsion and stabilizes intermolecular packing, thus increasing ΔH_m^{cores}.
2) When the π systems are polarized, like polarizations repel and opposite polarizations attract. An alternation of electron-poor and electron-rich π system along the strand is thus recommended for producing intermolecular self-cohesion and large ΔH_m^{cores}.

These points are at the origin of the empirical rule of thumb proposed by Nguyen and co-workers in the context of banana-shaped mesogens; Nguyen et al. claim that an alternate polarization of successive aromatic rings along bent strands strongly favors mesomorphism in the final materials, as illustrated in $\mathbf{L3}^{C12}$ ($Cr \xrightarrow{157\,^\circ C} SmC \xrightarrow{162\,^\circ C} N \xrightarrow{168\,^\circ C} I$).[12] Inter-

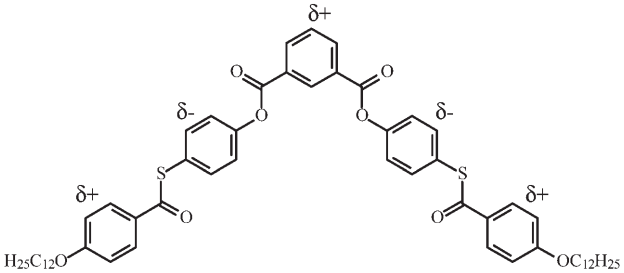

$\mathbf{L3}^{C12}$ $Cr \xrightarrow{157\,^\circ C} SmC \xrightarrow{162\,^\circ C} N \xrightarrow{168\,^\circ C} I$

estingly, the recent induction of mesomorphism in the bent complexes $[Ln(\mathbf{L4}^{C12})(NO_3)_3]$ along the lanthanide series (Ln = La–Lu) might be ascribed to similar electrostatic considerations (Scheme 1a).[9c,d] To explore the origins and the consequences of an alternation of electrostatic aromatic polarizations along the ligand strands on 1) the intermolecular interactions and 2) the formation of thermotropic liquid-crystalline phases, we have synthesized the isomeric ligand $\mathbf{L5}^{C12}$ and its complexes $[Ln(\mathbf{L5}^{C12})(NO_3)_3]$, in which the ester spacers are reversed (Scheme 1b). A deeper understanding of the electronic structures combined with the explicit modeling of the electrostatic potential at the surface of the molecule may help in rationalizing intermolecular cohesion forces between aromatic cores and, eventually, ΔH_m^{cores}. The recent use of predictable aromatic donor–acceptor π–π stacking interactions between hemidisk molecules for building homo- and heteroleptic columns in columnar mesophases is related to the same global approach,[13] as are the switches between nematic and smectic organizations observed upon inversion of the ester spacers in thermotropic polyaromatic 1,1′-disubstituted ferrocene-containing liquid crystals and in extended dicatenar bipyridines.[14]

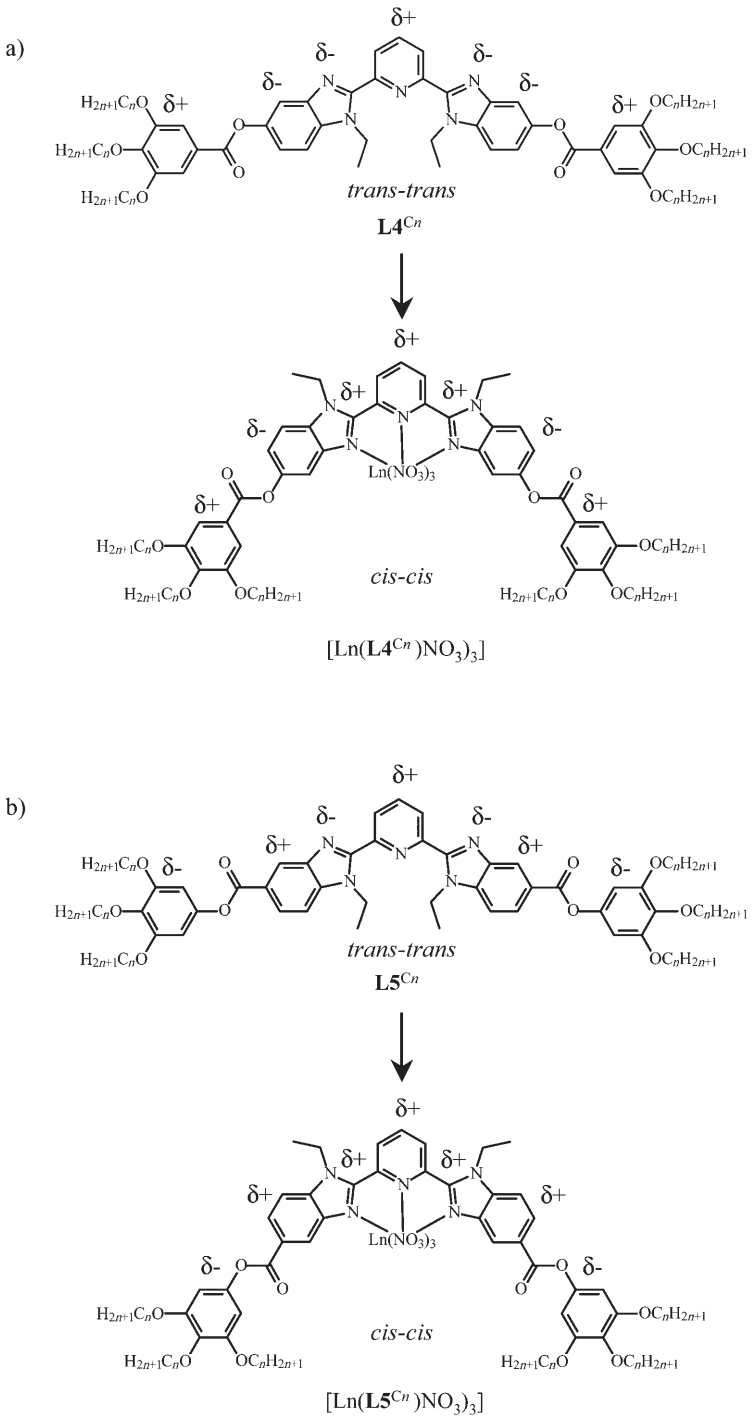

Scheme 1. Schematic structures, conformations, and polarizations of the tridentate ligands a) $\mathbf{L4}^{Cn}$ and b) $\mathbf{L5}^{Cn}$, and of their complexes with $Ln(NO_3)_3$.

Results

Syntheses and molecular structures of the ligands $\mathbf{L5}^{Cn}$ (n=0, 1, 12): A mild and selective $KMnO_4$ oxidation performed under catalytic phase-transfer conditions,[15] followed by alkaline hydrolysis transform the starting tridentate unit 2,6-bis(1-ethyl-5-methoxymethyl-benzimidazol-2-yl)pyridine (**1**)[6] into 2,6-bis(1-ethyl-5-carboxy-benzimidazol-2-yl)pyridine (**3**) (Scheme 2). The preparation of the air-sensitive electron-rich substituted tetraphenol partner **6** is more delicate and requires a careful Grignard reduction of the gallic ester **4**,[9d] followed by a Baeyer–Villiger type oxidative rearrangement, eventually leading to the target tetraphenol **6**.[16] The coupling of the central tridentate binding unit **3** with two appended tetraphenols **6** in the presence of 1-[3-(dimethylamino)propyl]-3-ethylcarbodiimide (EDCI) and 4-(diethylamino)pyridine (DMAP) yields the extended rodlike ligands $\mathbf{L5}^{Cn}$, which possess reversed ester spacers compared with the isomeric ligands $\mathbf{L4}^{Cn}$ (Scheme 1).[9d]

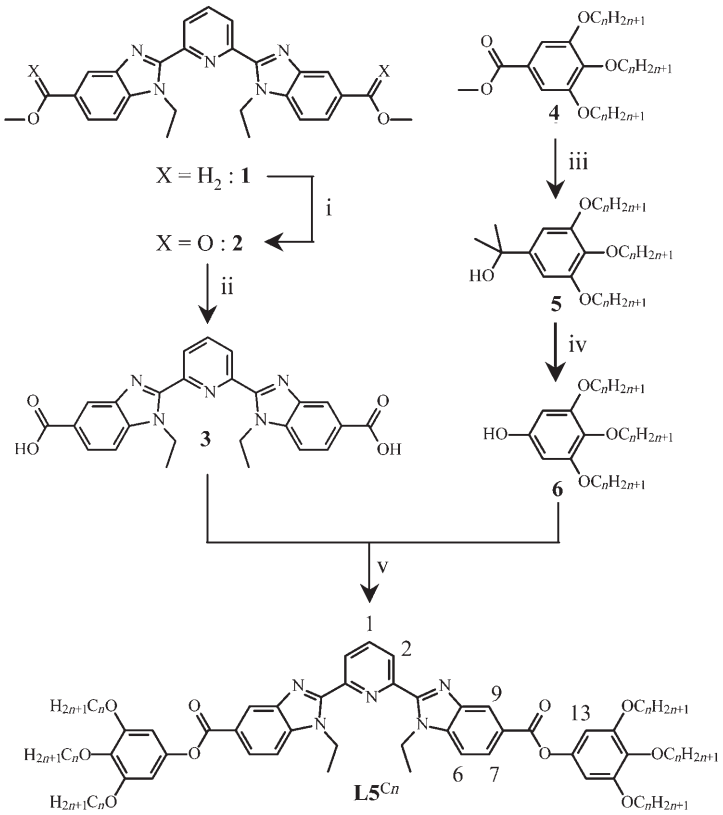

Scheme 2. Reagents: i) $KMnO_4$, TEBAC, CH_2Cl_2, 71%; (ii) KOH, EtOH, 100%; iii) CH_3MgI, Et_2O, 90% ($n=12$); iv) $NaBO_3$, BF_3-Et_2O, THF, 81% ($n=12$); v) EDCI, 4-DMAP, CH_2Cl_2, 71% ($n=12$).

Table 1. ^{1}H NMR chemical shifts [ppm] of the aromatic protons in $\mathbf{L}i^{C12}$ and $[Lu(\mathbf{L}i^{C12})(NO_3)_3]$ ($i=4$, 5) in CD_2Cl_2 at 298 K (numbering in Scheme 2).

	H1	H2	H6	H7	H9	H13
$\mathbf{L4}^{C12}$	8.05	8.32	7.48	7.18	7.64	7.43
$\mathbf{L5}^{C12}$	8.19	8.51	7.67	8.25	8.73	6.53
$[Lu(\mathbf{L4}^{C12})(NO_3)_3]$	8.51	8.23	7.65	7.41	8.12	7.52
$[Lu(\mathbf{L5}^{C12})(NO_3)_3]$	8.57	8.31	7.75	8.37	9.16	6.62

The ^{1}H NMR spectra of $\mathbf{L4}^{C12}$ and $\mathbf{L5}^{C12}$ display six aromatic CH signals (H1, H2, H6, H7, H9, H13, numbering in Scheme 2) and one enantiotopic A_2X_3 spin system for the ethyl residue connected to the benzimidazole ring, compatible with dynamically average C_{2v} symmetry for the aromatic rigid core on the NMR timescale (Table 1). The lack of NOE effects between the methylene group and H2 confirms a *trans–trans* arrangement of the 2,6-bis(benzimidazol-2-yl)pyridine unit (Scheme 1),[6,9d] while the strong diamagnetic shielding of H13 ($\Delta\delta=-0.90$ ppm) and the concomitant deshielding of H6 ($\Delta\delta=+0.19$ ppm), H7 ($\Delta\delta=$ 1.07 ppm), and H9 ($\Delta\delta=+$ 1.09 ppm, Table 1) on going from $\mathbf{L4}^{C12}$ to $\mathbf{L5}^{C12}$ support the intuitive polarization of the aromatic groups depicted in Scheme 1. On the other hand, the pyridine protons H1 and H2 are detected at low field for both ligands, in agreement with their connection to an electron-poor pyridine ring, which is not significantly affected by the orientation of the ester spacers.

In agreement with NOE measurements recorded in solution, the crystal structures of the tridentate synthon **2** (Figure 1a) and of the ligand $\mathbf{L5}^{C1}$ (Figure 1b) show the aromatic 2,6-bis(benzimidazol-2-yl)pyridine units to adopt the usual *trans–trans* arrangement (i.e. both N2 and N4 atoms adopt a trans orientation with respect to N1, Scheme 1 and Figure 1).[6,9d] This conformation provides an approximate rodlike shape for the tridentate rigid core with small deviations from planarity between the aromatic rings (interplanar pyridine benzimidazole–pyridine angles: 20.2° in **2** and 11.1–13.9° in $\mathbf{L5}^{C1}$, Tables S1 and S2, Supporting Information). Interestingly, the carbonyl group of the spacer is coplanar with the aromatic ring to which it is attached, which produces a contrasting situation for $\mathbf{L4}^{C1}$ and $\mathbf{L5}^{C1}$, because the carbonyl group is almost perpendicular to the benzimidazole ring in $\mathbf{L4}^{C1}$ (interplanar angle = 63.9–68.0°),[9d] but coplanar with this ring in $\mathbf{L5}^{C1}$ (interplanar angle = 5.2–8.8°, Figure 1, Table S2 and Figure S1 Supporting Information). However, the electrostatic repulsion operating between the carbonyl group and the phenol derivative to which it is connected, produces similar cross-hatched organization of the appended

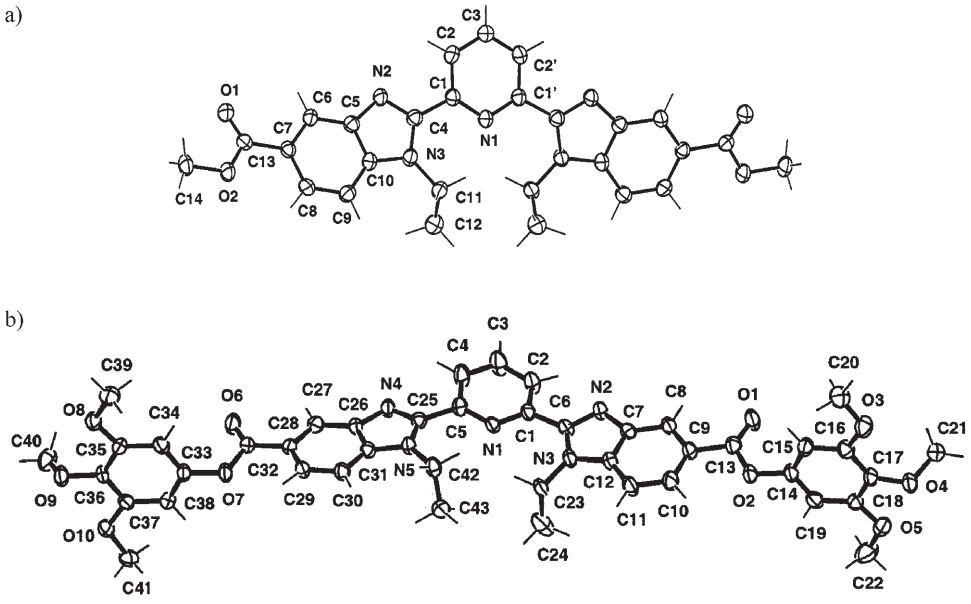

Figure 1. Views of the tridentate ligands in the crystal structures of a) **2** and b) $\mathbf{L5}^{C1}\cdot 0.5\,CH_2Cl_2$ with numbering schemes. Ellipsoids are represented at the 50% probability level.

phenyl rings with respect to the central tridentate binding unit in $\mathbf{L4}^{C1}$ (interplanar benzimidazole–phenyl angles = 68.8–75.5°)[9d] and in $\mathbf{L5}^{C1}$ (interplanar benzimidazole–phenyl angle = 83.1–89.4°, Figure 1 and Table S2, Supporting Information). Consequently, except for the orientation of the ester spacers, the molecular structures of $\mathbf{L4}^{C1}$ and $\mathbf{L5}^{C1}$ are almost superimposable (Figure S1, Supporting Information), and the bond lengths and bond angles are standard.[17] A close scrutiny at the aromatic C–C bonds in $\mathbf{L4}^{C1}$ and $\mathbf{L5}^{C1}$ shows only marginal differences, which cannot be considered as probes for electrostatic polarization along the strand (Table S3, Supporting Information).

In the crystal structure of $\mathbf{L4}^{C1}$, we have previously shown that each molecule is involved in four intermolecular π–π stacking interactions: two benzimidazole–phenyl (interplanar angle = 18.4°, d = 3.34 Å), one phenyl–phenyl (interplanar angle = 0°, d = 3.67 Å), and one benzimidazole–benzimidazole (interplanar angle = 0°, d = 3.56 Å).[9d] In the crystal structure of the isomeric ligand $\mathbf{L5}^{C1}$, we also observe four intermolecular π–π interactions responsible for the crystal packing: two benzimidazole–benzimidazole (interplanar angle = 11.3°, d = 3.43 Å, Figure S2, Supporting Information) and two pyridine–benzimidazole (interplanar angle = 13.9°, d = 3.68 Å, Figure S2, Supporting Information). It is worth noting that the terminal electron-rich substituted tetraphenol rings in $\mathbf{L5}^{C1}$ are not involved in phenyl–phenyl π-stacking interactions, while the related, but electron-poor, gallic acids in $\mathbf{L4}^{C1}$ participate in intermolecular packing, in agreement with the basic rules established for the stabilization of interacting π systems.[11] According to the same rules, the interactions between electron-poor benzimidazole rings occur at short distances in both ligands $\mathbf{L5}^{C1}$ and $\mathbf{L4}^{C1}$ (Figure S2, Supporting Information), and in the intermediate **2** (Figure S3, Supporting Information). Altogether, each isomer $\mathbf{L4}^{C1}$ and $\mathbf{L5}^{C1}$ takes part in four intermolecular stacking interactions, which ensure comparable cohesion of the rigid cores in the solid state.

Ground-state electronic structures and thermal properties of the ligands $\mathbf{L5}^{Cn}$, (n = 0, 1, 12): To explore the origin of the intermolecular interactions involving the aromatic rings along the ligand strands and to further rationalize photophysical properties, we have performed time-dependent DFT (TD-DFT) calculations for unraveling the electronic structure of the ground state, together with the lowest ligand-centered singlet and triplet excited states. The molecular structure of $\mathbf{L4}^{C1}$ and $\mathbf{L5}^{C1}$ optimized in the gas phase, are very similar to those observed in the crystal structures, and Figure 2 shows selected Kohn–Sham orbitals lying close to the HOMO–LUMO gap. The associated computed energies of the 120 lowest singlet and triplet electronic states, together with their energy diagrams are given in Tables S4, S5, and in Figure S4 (Supporting Information).

The atomic charges have been fitted to reproduce the electrostatic potentials calculated according to the Merz–Singh–Kollmann scheme (Tables S6 and S7, Supporting Information).[18] The molecular electrostatic potentials (MEP)

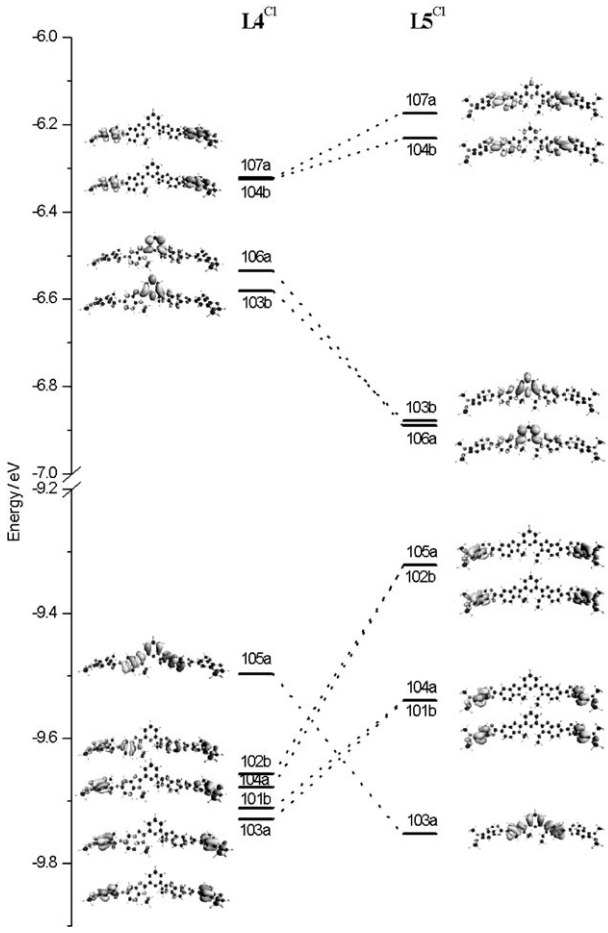

Figure 2. Walsh diagram for selected Kohn–Sham orbitals close to the HOMO–LUMO gap in ligands $\mathbf{L4}^{C1}$ and $\mathbf{L5}^{C1}$. Energies are given in eV (1 eV = 8065.5 cm^{-1}).

have been calculated for sets of 3D points corresponding to the Connolly surfaces for $\mathbf{L4}^{C1}$ and $\mathbf{L5}^{C1}$ and are shown in Figure 3. Both potentials (MEP) display an electron-deficient pyridine ring connected to electron-rich benzimidazole

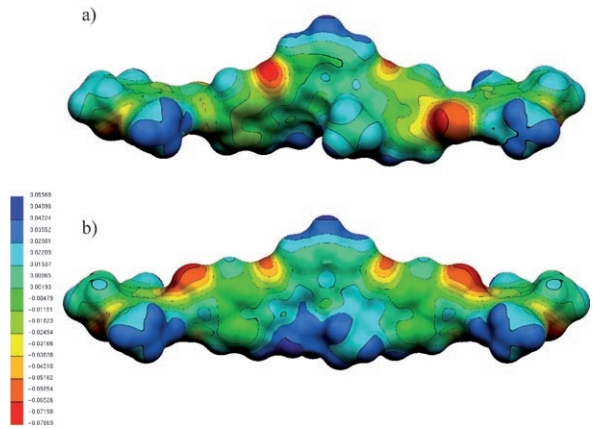

Figure 3. Color-coded representation of DFT molecular electrostatic potentials (MEP) computed on the Connolly surfaces around a) $\mathbf{L4}^{C1}$ and b) $\mathbf{L5}^{C1}$ in their optimized gas phase geometries. MEP values are given in atomic units.

rings. The major difference between the two ligands concerns the terminal phenyl rings, which display a more negative potential for $\mathbf{L5}^{C1}$ than for $\mathbf{L4}^{C1}$, in agreement with intuitive polarization derived from standard electronic effects brought by the substituents connected to the aromatic rings (Scheme 1). However, the differences in the electrostatic potentials for $\mathbf{L4}^{C1}$ and $\mathbf{L5}^{C1}$ remain faint and marginal (Figure 3), and we predict only minor variations in the intermolecular electrostatic interactions operating in condensed phases, as exemplified by the packing observed in the crystal structures of $\mathbf{L4}^{C1}$ and $\mathbf{L5}^{C1}$. It is thus not surprising that the hexagonal columnar mesophase Col_h detected in the temperature range 40–71° for $\mathbf{L5}^{C12}$ (characterized by differential scanning calorimetry (DSC, Table 2) and small-angle X-ray scattering (SAXS, Table S8, Supporting Information) resembles that previously described for $\mathbf{L4}^{C12}$ (hexagonal columnar mesophase Col_h in the temperature range 25–61°, Table 2).[9d]

Table 2. Phase-transition temperatures with enthalpy and entropy changes, and geometrical characteristics of the mesophases for the ligands $\mathbf{L5}^{C12}$, $\mathbf{L6}^{C12}$, and their complexes $[Lu(\mathbf{L5}^{C12})(NO_3)_3]$ and $[Lu(\mathbf{L6}^{C12})(NO_3)_3]$.

	Transition[a]	T [°C]	ΔH [kJ mol^{-1}]	ΔS [J mol^{-1} K^{-1}]	Geometrical parameters	Ref.
$\mathbf{L4}^{C12}$	Cr→g	0	[b]	[b]		[9d]
	g→Col_h	25	[b]	[b]	a=42.40 Å	
	Col_h→I	61	3.3	10	S=1555 Å^2	
$\mathbf{L5}^{C12}$	g→Col_h	40	[b]	[b]	a=41.69 Å	this work
	Col_h→I	71	4.0	12	S=1505 Å^2	
$\mathbf{L6}^{C12}$	Cr→Col_h	93	29.8	81	a=54.21 Å	this work
	Col_h→I	159	3.8	9	S=2545 Å^2	
$[Lu(\mathbf{L4}^{C12})(NO_3)_3]$	g→Col_h	160	[b]	[b]	a=31.20 Å	[9d]
	Col_h→Dec	223			S=842 Å^2	
$[Ln(\mathbf{L5}^{C12})(NO_3)_3]$	g→I	120–130	[b]	[b]		this work
	I→Dec	230				
$[Lu(\mathbf{L6}^{C12})(NO_3)_3]$	g→Col_h	170	[b]	[b]	a=31.38 Å	this work
	Col_h→I/dec	250			S=853 Å^2	

[a] Cr=crystal, g=glass, Col_h=hexagonal columnar phase, I=isotropic fluid; first-order transition temperatures are given as the onset of the peak observed during the second heating processes (Seiko DSC 220C differential scanning calorimeter, 5 °C min^{-1}, under N_2); the liquid crystalline phases were identified from their optical textures and from SAXS studies. [b] Glass transition determined by polarizing light microscopy (PLM).

Syntheses, molecular structures, and thermal properties of the complexes $[Ln(\mathbf{L5}^{Cn})(NO_3)_3]$ (Ln=Sm–Lu): The mixing of stoichiometric quantities of $\mathbf{L5}^{C12}$ (1 equiv) in dichloromethane with $Ln(NO_3)_3{\cdot}x\,H_2O$ (1 equiv, x=2–4, Ln=Sm–Lu) in acetonitrile gives 80% of microcrystalline powders, the elemental analyses of which correspond to $[Ln(\mathbf{L5}^{C12})(NO_3)_3]{\cdot}n H_2O$ (Ln=Sm, n=3.5, **7**; Ln=Eu, n=2.5, **8**; Ln=Gd, n=3, **9**; Ln=Tb, n=0, **10**; Ln=Dy, n=0, **11**; Ln=Ho, n=1.5, **12**; Ln=Er, n=0, **13**; Ln=Tm, n=1, **14**; Ln=Yb, n=0.5, **15**; Ln=Lu, n=1.5, **16**; Table S9, Supporting Information). For the larger Ln^{III} (Ln=La–Nd), mixtures of complexes can be precipitated, in which a significant excess of ligand is detected (with respect to the expected 1:1 stoichiometry). These last complexes have both been investigated further in this contribution. Moreover, we were unable to obtain monocrystals for the lipophilic complexes $[Ln(\mathbf{L5}^{C12})(NO_3)_3]$ (**7**–**16**), but two model complexes $[Eu(\mathbf{2})(NO_3)_3(H_2O)]{\cdot}CH_3NO_2$ (**17**) and $[Yb(\mathbf{L5}^{C0})(NO_3)_3]{\cdot}2\,CH_3CN$ (**18**) possessing less lipophilic ligands, provided X-ray quality prisms by slow diffusion of diethyl ether into concentrated solutions of the complexes in nitromethane and in acetonitrile, respectively. Both crystal structures are made up of neutral complexes $[Eu(\mathbf{2})(NO_3)_3(H_2O)]$ and $[Yb(\mathbf{L5}^{C0})(NO_3)_3]$, together with non-coordinated solvent molecules. The molecular structures of these complexes display a similar *cis–cis* 2,6-bis(benzimidazol-2-yl)pyridine aromatic core acting as a roughly planar meridional tridentate ligand (Figure 4, interplanar pyridine-benzimidazole angles=4.3–15.2°, Tables S10 and S11, Supporting Information).

The Ln–O and Ln–N distances are standard (Table 3).[9d] By using Shannon's definition[19] and $r(N)$=1.46 Å, $r(O_{water})$=1.35 Å and $r(O_{nitrate})$=1.31 Å,[20] we calculate $R_{Eu}^{CN=10}$=1.187 Å in **17** and $R_{Yb}^{CN=9}$=1.044 Å in **18**, in good agreement with related ionic radii reported for the analogous complexes $[Eu(\mathbf{L4}^{C0})(NO_3)_3(CH_3CN)]$ ($R_{Eu}^{CN=10}$=1.142 Å) and $[Yb(\mathbf{L4}^{C0})(NO_3)_3]$ ($R_{Yb}^{CN=9}$=1.046 Å), in which the lanthanides are similarly ten- and nine-coordinated, respectively.[9d] The detailed arrangement of the bidentate nitrate groups around Ln^{III} is slightly different on going from **18** to **17** in order to accommodate the extra water molecule around Eu^{III} (Figure 4 and Figure S5a, Supporting Information). However, each pair of ten-coordinate complexes $[Eu(\mathbf{L4}^{C0})(NO_3)_3(CH_3CN)]$ and $[Eu(\mathbf{2})(NO_3)_3(H_2O)]$ (Figure S5b), and of nine-coordinate complexes $[Yb(\mathbf{L4}^{C0})(NO_3)_3]$ and $[Yb(\mathbf{L5}^{C0})(NO_3)_3]$ (Figure S5c, Supporting Information) are almost superimposable, except for the orientation of the carbonyl groups of the spacer, which are systematically coplanar with the aromatic ring to which they are connected, as

Table 3. Selected bond lengths [Å] and bite angles [°] in $[Eu(\mathbf{2})(NO_3)_3(H_2O)]$ (**17**) and $[Yb(\mathbf{L5}^{C0})(NO_3)_3]$ (**18**).

	17	**18**		**17**	**18**
Ln–N1	2.657(2)	2.501(2)	Ln–O1b	2.521(2)	2.435(2)
Ln–N2	2.510(2)	2.402(2)	Ln–O2b	2.644(2)	2.348(2)
Ln–N4	2.488(2)	2.400(2)	Ln–O1c	2.554(2)	2.353(2)
Ln–O1a	2.526(2)	2.393(2)	Ln–O2c	2.470(2)	2.438(2)
Ln–O2a	2.542(2)	2.370(2)	Ln–O1w	2.444(2)	–
N1-Ln-N2	62.97(6)	65.76(7)	O1a-Ln-O2a	50.21(6)	54.14(7)
N1-Ln-N4	62.86(7)	65.84(7)	O1b-Ln-O2b	49.27(7)	53.19(9)
N2-Ln-N4	125.78(7)	131.37(7)	O1c-Ln-O2c	51.08(7)	53.01(8)

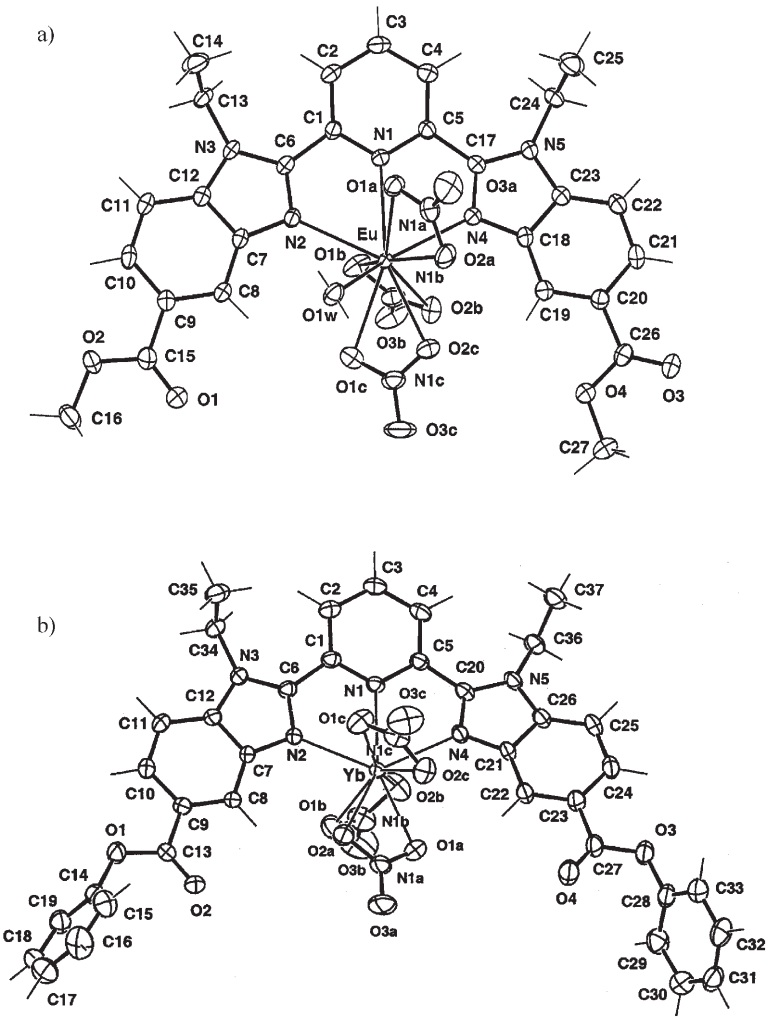

Figure 4. Views of a) [Eu(**2**)$(NO_3)_3(H_2O)$] in the crystal structure of **17** and b) [Yb($\mathbf{L5}^{C0}$)$(NO_3)_3$] in the crystal structure of **18** with numbering schemes. Ellipsoids are represented at the 50% probability level.

previously described for the free ligands (i.e., phenyl for $\mathbf{L4}^{C0}$ and benzimidazole for $\mathbf{L5}^{C0}$).

The intermolecular interactions for [Eu(**2**)$(NO_3)_3(H_2O)$] (**17**) in the solid state are limited to one pair of benzimidazole–benzimidazole π stacking (interplanar angle = 4.2°, d = 3.69 Å, Figure S6, Supporting Information). However, the extended aromatic strands in [Yb($\mathbf{L5}^{C0}$)$(NO_3)_3$] (**18**) produces two different types of intermolecular π-stacking interactions involving pyridine and phenyl rings on one hand (interplanar angle = 14.7°, d = 3.70 Å), and pairs of benzimidazole rings (interplanar angle = 10.8°, d = 3.80 Å) on the other hand (Figure S7, Supporting Information). As previously noted, in the crystal structure of $\mathbf{L5}^{C1}$, the terminal electron-rich tetraphenol rings do not show self-complementarity for intermolecular π stacking, in contrast to the closely related efficient intermolecular interactions occurring between pairs of electron-poor gallic acid residues in [Yb($\mathbf{L4}^{C0}$)$(NO_3)_3$] (interplanar angle = 0°, d = 3.36 Å).[9d] Altogether, each [Yb($\mathbf{L5}^{C0}$)$(NO_3)_3$] complex in **18** is involved in four intermolecular π-stacking interactions (two benzimidazole–benzimidazole and two pyridine–phenyl), whereas [Yb($\mathbf{L4}^{C0}$)$(NO_3)_3$] displays six related interactions (four benzimidazole–benzimidazole and two phenyl–phenyl).[9d] We reasonably deduce that the intermolecular cohesion between the aromatic cores in the solid state is larger for the complexes [Ln($\mathbf{L4}^{Cn}$)$(NO_3)_3$], a prediction which is supported by the melting processes occurring around 120–130 °C for [Ln($\mathbf{L5}^{C12}$)$(NO_3)_3$] after the removal of the interstitial water molecules (Table 3) and around 140–160 °C for [Ln($\mathbf{L4}^{C12}$)$(NO_3)_3$].[9d] Moreover, the melting process in the last complexes leads to organized cubic or columnar hexagonal mesophases, in which significant directional intermolecular interactions between the polarized cores operate.[9d] For [Ln($\mathbf{L5}^{C12}$)$(NO_3)_3$] (Ln = Sm–Lu), the melting and clearing processes coincide, thus leading to the isotropic liquid, in which any directional intermolecular interactions are removed. The behavior of [Ln($\mathbf{L5}^{C12}$)$(NO_3)_3$] in isotropic medium has been studied in CH_2Cl_2:CH_3CN (1:1) solvent mixtures. Spectrophotometric titrations of $\mathbf{L5}^{C12}$ (10^{-4} M) with $Ln(NO_3)_3{\cdot}x\,H_2O$ (x = 2–4, Ln = Eu, Y, Lu) in the range Ln:$\mathbf{L5}^{C12}$ = 0.1–2.0 show a single end point for Ln:$\mathbf{L5}^{C12}$ = 1.0 (Figure S8, Supporting Information), as previously reported for $\mathbf{L4}^{C12}$ in the same conditions.[9d] The experimental data can be satisfyingly fitted with non-linear least-squares techniques[21] to the equilibrium shown in Equation (1) (Table 4).

$$\mathbf{L5}^{C12} + Ln(NO_3)_3 \rightleftharpoons [Ln(\mathbf{L5}^{C12})(NO_3)_3] \qquad \beta_{11}^{Ln\text{-}\mathbf{L5}C12} \qquad (1)$$

Comparisons between $\log(\beta_{11}^{Ln})$ obtained for [Ln($\mathbf{L}i^{C12}$)$(NO_3)_3$] (i = 4, 5) in the same conditions show only a marginal stabilization for the complexes with $\mathbf{L5}^{C12}$ (Table 4), and we conclude that the reverse orientation of the ester spacers has negligible effect on the affinity of the ligands for Ln^{III}.

The ^{1}H NMR spectrum of [Lu($\mathbf{L5}^{C12}$)$(NO_3)_3$] shows the expected formation of a monomeric complex displaying dynamically average C_{2v} symmetry on the NMR time scale (6 CH aromatic signals and one quartet for the enantiotopic methylene protons connected to the benzimidazole rings,

Table 4. Stability constants obtained for the formation of the complexes $[Ln(\mathbf{L}i^{C12})(NO_3)_3]$ ($i=4$, 5) in CH_2Cl_2:CH_3CN (1:1) at 293 K.

Ln	$R_{Ln}^{CN=9}$ [Å][a]	$\log(\beta_{11}^{Ln\text{-}\mathbf{L}4C12})$[b]	$\log(\beta_{11}^{Ln\text{-}\mathbf{L}5C12})$
Eu	1.12	5.3 (2)	6.3(1)
Y	1.08	5.9 (1)	6.3(2)
Lu	1.03	6.1 (1)	6.4(4)

[a] Ionic radius for nine-coordinate Ln^{III}.[19] [b] Taken from reference [9d].

Table 1 and Figure S9a, Supporting Information), as previously established for the related complex $[Lu(\mathbf{L}4^{C12})(NO_3)_3]$.[22] The protons H13, attached to the terminal phenyl ring, is drastically shielded ($\Delta\delta=-0.9$ ppm) on going from $[Lu(\mathbf{L}4^{C12})(NO_3)_3]$ to $[Lu(\mathbf{L}5^{C12})(NO_3)_3]$, while H9 is concomitantly deshielded ($\Delta\delta=+1.04$ ppm) as a result of the connection of the attracting carbonyl group to the benzimidazole ring in the latter complex (numbering is given in Scheme 2). It is therefore tempting to consider these strong variations in the NMR shifts as direct probes for assigning specific electronic densities in the aromatic rings of $[Lu(\mathbf{L}4^{C12})(NO_3)_3]$ and $[Lu(\mathbf{L}5^{C12})(NO_3)_3]$. However, a close scrutiny at the crystal structures of $[Yb(\mathbf{L}5^{C0})(NO_3)_3]$ (Figure 4b) shows that the coplanar arrangement of the carbonyl group and the benzimidazole ring puts H9 in the deshielding region of the C=O moiety.[23] This effect may easily overcome standard inductive effects. Moreover, ring current in cyclic conjugated π-system is also known to balance opposite inductive effects, because an increased electron density in the aromatic ring results in a deshielding of the aromatic protons due to local diamagnetic anisotropies.[23] We conclude that the ^{1}H NMR shifts of the aromatic protons in $[Lu(\mathbf{L}4^{C12})(NO_3)_3]$ and in $[Lu(\mathbf{L}5^{C12})(NO_3)_3]$ can be hardly used as a safe guide for probing electron densities in the aromatic rings, and intuitive deductions (Scheme 1) must be confirmed by DFT calculations. Interestingly, the ^{1}H NMR spectrum of the analogous complex $[Eu(\mathbf{L}5^{C12})(NO_3)_3]$, in which Yb^{III} has been replaced with the larger Eu^{III} cation, shows the coexistence of two different complexes in thermodynamic equilibrium according to Equation (2) (Figure S9, Supporting Information), which corresponds to the dimerization process previously established for $[Eu(\mathbf{L}4^{C12})(NO_3)_3]$ in the same conditions.[9d]

$$2\,[Eu(\mathbf{L}5^{C12})(NO_3)_3] \rightleftharpoons [Eu_2(\mathbf{L}5^{C12})_2(NO_3)_6] \qquad K_d^{Eu\text{-}\mathbf{L}5C12} \tag{2}$$

This mechanism is supported by the experimental ratio of the auto-diffusion coefficients $D_{mono}/D_{dimer}=1.3(1)$ deduced from NMR diffusion measurements in CD_2Cl_2,[24] which translates [Eq. (3)] into a ratio of molecular weights $MM_{dimer}/MM_{mono}=2.2(1)$ close to 2.0, the value predicted by equilibrium (2) (it is assumed that the specific partial volumes of the two complexes are similar $\tilde{\nu}_{mono}\approx\tilde{\nu}_{dimer}$).[9d]

$$\frac{D_{dimer}}{D_{mono}}=\sqrt[3]{\frac{\tilde{\nu}_{mono}\cdot MM_{mono}}{\tilde{\nu}_{dimer}\cdot MM_{dimer}}} \tag{3}$$

Variable-temperature NMR data in CD_2Cl_2 (273–313 K) show that the $[Eu_2(\mathbf{L}5^{C12})_2(NO_3)_6]/[Eu(\mathbf{L}5^{C12})(NO_3)_3]$ ratio smoothly decreases with increasing temperature, thus leading to dimerization constants $K_d^{Eu\text{-}\mathbf{L}5C12}=|\,dimer\,|/|\,mono\,|^2$ [Eq. (2)], which match a linear van't Hoff plot with $\Delta H_d^{Eu\text{-}\mathbf{L}5C12}=-27(2)$ kJ·mol^{-1} and $\Delta S_d^{Eu\text{-}\mathbf{L}5C12}=-98(4)$ J mol^{-1} K^{-1} [Eq. (4)].

$$-R\ln(K_d^{Eu\text{-}\mathbf{L}iC12})=\frac{\Delta H_d^{Eu\text{-}\mathbf{L}iC12}}{T}-\Delta S_d^{Eu\text{-}\mathbf{L}iC12} \tag{4}$$

The thermodynamic data obtained for $[Eu(\mathbf{L}5^{C12})(NO_3)_3]$ significantly differ from $\Delta H_d^{Eu\text{-}\mathbf{L}4C12}=-54(4)$ kJ mol^{-1} and $\Delta S_d^{Eu\text{-}\mathbf{L}4C12}=-162(16)$ J mol^{-1} K^{-1} reported for $[Eu(\mathbf{L}4^{C12})(NO_3)_3]$ in the same conditions.[9d] We ascribe the dramatic decrease of the enthalpic driving force of the dimerization process transforming $[Eu(\mathbf{L}5^{C12})(NO_3)_3]$ into $[Eu_2(\mathbf{L}5^{C12})_2(NO_3)_6]$, to the coplanar orientation of the carbonyl groups of the ester spacers with the benzimidazole rings (Figure 4b and Figure S5c, Supporting Information), which hinders the approach of the second complex when forming the double nitrate bridge in the dimer.[9d]

Ground state electronic structures of the complexes $[Ln(\mathbf{L}4^{Cn})(NO_3)_3]$ and $[Ln(\mathbf{L}5^{Cn})(NO_3)_3]$ (Ln = Eu, Gd, Tb, Lu): The geometries of the complexes $[Lu(\mathbf{L}4^{C1})(NO_3)_3]$ and $[Lu(\mathbf{L}5^{C1})(NO_3)_3]$ optimized by DFT in the gas phase show the expected *cis–cis* orientation of the bound 2,6-bis(benzimidazol-2-yl)pyridine unit resulting from its meridional tricoordination to Lu^{III}. The gas-phase and solid-state geometries are similar except for a less pronounced cross-hatched arrangement of the appended phenyl rings with respect to the central tridentate unit (Figure S10, Supporting Information). Figure 5 shows selected Kohn–Sham orbitals lying close to the HOMO–LUMO gap, and the associated computed energies of the 120 lowest singlet and triplet electronic states, together with their energy diagrams are given in Tables S12 and S13 (Supporting Information).

We have also calculated the DFT fitted atomic charges according to the Merz–Singh–Kollman scheme (Tables S14, and S15, Supporting Information)[18] and the MEP on the Connolly surface (Figure 6) for $[Lu(\mathbf{L}i^{C1})(NO_3)_3]$ ($i=4$, 5). Compared with the same approach applied to the free ligands (Figure 3), the complexation to $Lu(NO_3)_3$ produces a clearer discrimination of the electrostatic potentials between a strongly positive region in the back of the 2,6-bis(benzimidazol-2-yl)pyridine core, and a strongly negative region around the metallic $Lu(NO_3)_3$ unit (Figure 6). A close scrutiny at the computed electrostatic potentials along the strand shows that the appended phenyl rings are more electron-rich in $[Lu(\mathbf{L}5^{C1})(NO_3)_3]$, while the coordinated tridentate aromatic core is more electron-deficient, as predicted by the intuitive charge assignment given in Scheme 1. Consequently, $[Lu(\mathbf{L}4^{C1})(NO_3)_3]$ possesses a larger number of polarization alternances (4) along the strand (phenyl(+)-phenyl(−)-

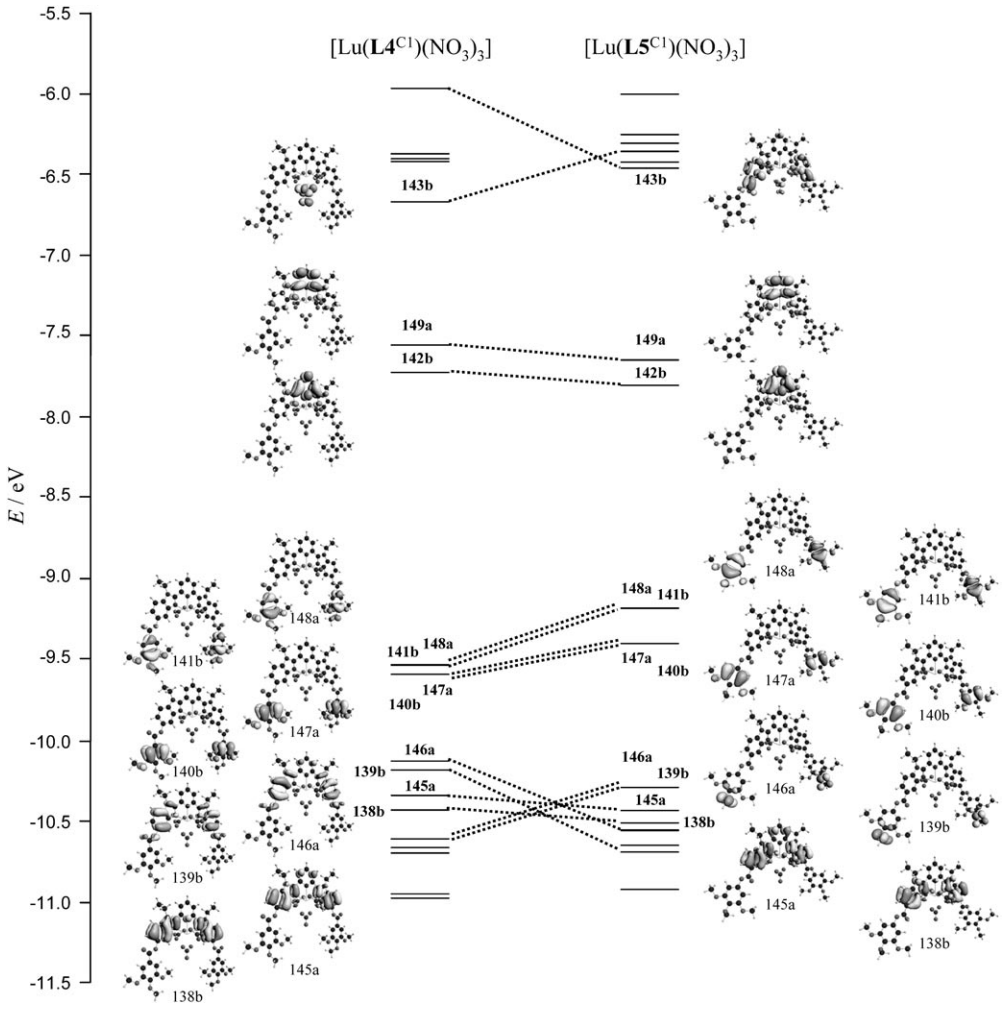

Figure 5. Walsh diagram for selected Kohn–Sham orbitals close to the HOMO–LUMO gap in the complexes [Lu($\mathbf{L4}^{C1}$)$(NO_3)_3$] and [Lu($\mathbf{L5}^{C1}$)$(NO_3)_3$]. Energies are given in eV (1 eV = 8065.5 cm^{-1}).

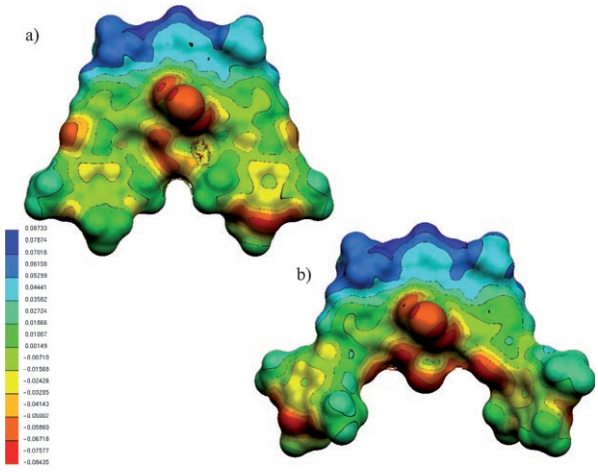

Figure 6. Color-coded representation of DFT MEP computed on the Connolly surfaces around a) [Lu($\mathbf{L4}^{C1}$)$(NO_3)_3$] and b) [Lu($\mathbf{L5}^{C1}$)$(NO_3)_3$] in their optimized gas-phase geometries. MEP values are given in atomic units.

imidazole(+)-pyridine(+)-imidazole(+)-phenyl(−)-phenyl(+), Scheme 1a and Figure 6a) than [Lu($\mathbf{L5}^{C1}$)$(NO_3)_3$] (2 alternances: phenyl(−)-phenyl(+)-imidazole(+)-pyridine(+)-imidazole(+)-phenyl(+)-phenyl(−), Scheme 1b and Figure 6b), which agrees with Nguyen's rule of thumb[12] for empirically justifying why the lipophilic analogue [Lu($\mathbf{L4}^{C12}$)$(NO_3)_3$] is mesogenic, while [Lu($\mathbf{L5}^{C12}$)$(NO_3)_3$] is not (Table 3). In terms of intermolecular packing involving the aromatic cores, the increased alternance of polarization along the strand maximizes the possibility of favorable π-stacking interactions occurring between the aromatic cores of closely spaced identical molecules. It thus helps in creating a thermodynamic micro-segregation between the melting processes associated with the flexible and the rigid parts of the packed molecules.

Consequences of the reversal connection of ester spacers on the excited states and photophysical properties of the ligands Li^{Cn} and of their complexes [Ln(Li^{Cn})$(NO_3)_3$] (i = 4, 5; Ln = Eu, Gd, Tb, Lu): When the donor oxygen atoms of the ester spacers are connected to the benzimidazole rings

in $\mathbf{L4}^{C1}$, the HOMO (105a) corresponds to a π-orbital centered on the tridentate binding unit (Figure 2, left). The second highest occupied orbital (SHOMO, 102b) still displays π character, but its location is shifted toward the peripheral aromatic rings, a trend that continues for the next highest occupied orbitals. On the other hand, the LUMO (103b) and SLUMO (106a) orbitals in $\mathbf{L4}^{C1}$ are π orbitals mainly centered on the pyridine ring. Consequently, the lowest allowed singlet–singlet electronic transition (105a→103b, Figure 2, left) mainly involves the 2,6-bis(benzimidazol-2-yl)pyridine core, and its calculated oscillating strength is significant (transition 5 in Table S4, Supporting Information). Upon reversal of the ester spacers in $\mathbf{L5}^{C1}$, the Walsh diagram clearly shows the expected destabilization of the π orbitals centered on the phenyl rings and the concomitant stabilization of those centered on the 2,6-bis(benzimidazol-2-yl)pyridine unit (Figure 2, right). Consequently, 1) the HOMO (105a) is centered on the lateral phenyl rings in $\mathbf{L5}^{C1}$, 2) the LUMO is still centered on the pyridine ring and 3) the HOMO–LUMO gap dramatically shrinks (Table S5, Figure S4b, Supporting Information). The associated excited states thus possess strong phenyl(HOMO)→pyridine(LUMO) charge-transfer character, which strictly limits overlap density and stabilizing exchange interactions.[25] We therefore predict negligible oscillating strengths for electronic transitions originating from high-energy filled orbitals centered on the appended side arms, and reaching low-energy empty orbitals centered on the pyridine ring (Table S5, Supporting Information). The low-energy part of the absorption and emission electronic spectra of $\mathbf{L5}^{C1}$ thus mainly reflects the allowed π→π* transitions centered on the tridentate binding units (103a→103b, Figure 2 right and transition 19 in Table S5, Supporting Information). If we now compare the computed energy of the latter transition with that of the related transition in $\mathbf{L4}^{C1}$ (105a→103b; transition 5 in Table S4, Supporting Information, Figure 2 left), we predict that the first intense low-energy electronic π→π* transition occurs only at slightly higher energy for $\mathbf{L5}^{C1}$ ($\Delta E = 335\ cm^{-1}$). Experimentally, the absorption spectra of the analogous lipophilic ligands $\mathbf{L}i^{C12}$ (i = 4, 5) in CH_3CN/CH_2Cl_2 (1:1) agree with this prediction since the maximum of the lowest π→π* envelope is centered at 30580 cm^{-1} for $\mathbf{L4}^{C12}$ and at 30865 cm^{-1} for $\mathbf{L5}^{C12}$ ($\Delta E = 285\ cm^{-1}$, Table 5, Figure 7a). TD-DFT calculations also show that the related "emissive" triplet excited states located on the tridentate binding unit arise at lower energy than the related singlet excited state (computed singlet–triplet energy gap between the two lowest excited states: $\Delta E^{S-T}(\mathbf{L4}^{C1}) = E(^1\pi\pi^*$, level 5 in Table S4$) - E(^3\pi\pi^*$, level 1 in Table S4, Supporting Information$) = 1970\ cm^{-1}$ and $\Delta E^{S-T}(\mathbf{L5}^{C1}) = E(^1\pi\pi^*$, level 19 in Table S5$) - E(^3\pi\pi^*$, level 17 in Table S5, Supporting Information$) = 3285\ cm^{-1}$. These characteristics dominate the experimental electronic emission spectra of both ligands with $E(^1\pi\pi^*) \approx 25000\ cm^{-1}$ (0–0 phonon band) and $E(^3\pi\pi^*) \approx 21000\ cm^{-1}$ (0–0 phonon band) for the lowest emitting excited states, which are mainly centered on the tridentate 2,6-bis(benzimidazol-2-yl)pyridine unit (Table 5, Figure 7b,c).[6,26]

Close scrutiny of the Kohn–Sham orbitals computed for the complexes $[Lu(\mathbf{L4}^{C1})(NO_3)_3]$ and $[Lu(\mathbf{L5}^{C1})(NO_3)_3]$ show negligible mixing of ligand- and metal-centered orbi-

Table 5. Ligand-centered absorption and emission properties for ligands $\mathbf{L}i^{C12}$ and for complexes $[Ln(\mathbf{L}i^{C12})(NO_3)_3]$ (i = 4, 5; Ln = Eu, Gd, Tb, Lu).[a]

Compound	Absorption [cm^{-1}] π→π*	ε [$M^{-1}cm^{-1}$]	Emission [cm^{-1}] $^1\pi\pi^*$	Emission [cm^{-1}] $^3\pi\pi^*$	Lifetime [ms] $\tau(^3\pi\pi^*)$
$\mathbf{L4}^{C12}$	34365	47200	26000 sh	20700 sh	431(5)
	30580	46900	24210	19765	44(2)
			23200 sh	18700	
			21700 sh		
$\mathbf{L5}^{C12}$	39215	82080	26810 sh	20600 sh	31(1)
	30865	48000	25940	20120	5.4(4)
			24539	18640	
				17400 sh	
$[Lu(\mathbf{L4}^{C12})(NO_3)_3]$	35088	39580	25160	21100 sh	98(2)
	32787	40280	24180	20265	
	27779	29920	23120 sh	19000	
				18330	
$[Lu(\mathbf{L5}^{C12})(NO_3)_3]$	39060	57180	26900 sh	21345	[d]
	31545	33080	26450		
	29100	26390	23500		
$[Gd(\mathbf{L4}^{C12})(NO_3)_3]$	35090	43120	25280 sh	[b]	[b]
	33113	43240	24200		
	28736	31000			
$[Gd(\mathbf{L5}^{C12})(NO_3)_3]$	39060	58000	25300 sh	[b]	[b]
	31450	33250	24150		
	28330	27100			
$[Eu(\mathbf{L4}^{C12})(NO_3)_3]$	35090	35560	22625	[c]	[c]
	33335	35010	21505		
	28330	25540			
$[Eu(\mathbf{L5}^{C12})(NO_3)_3]$	39065	57180	23560	[c]	[c]
	31450	33030	22250		
	28330	27490	20555		
$[Tb(\mathbf{L4}^{C12})(NO_3)_3]$	35090	40350	22830	[c]	[c]
	33010	39650			
	28650	27540			
$[Tb(\mathbf{L5}^{C12})(NO_3)_3]$	39370	57260	23420	19120	[d]
	31150	31780	22270		
	27930	27800			

[a] Absorption spectra recorded for 10^{-4} M solution in CH_3CN/CH_2Cl_2 (1:1) at 295 K. Luminescence and lifetime data at 77 K. sh = shoulder. [b] Quenched by traces of Eu^{III} and Tb^{III}, see text.[30] [c] $^3\pi\pi^*$ luminescence quenched by transfer to Ln ion. [d] The weak luminescence intensity prevented determination of reliable luminescence decay times.

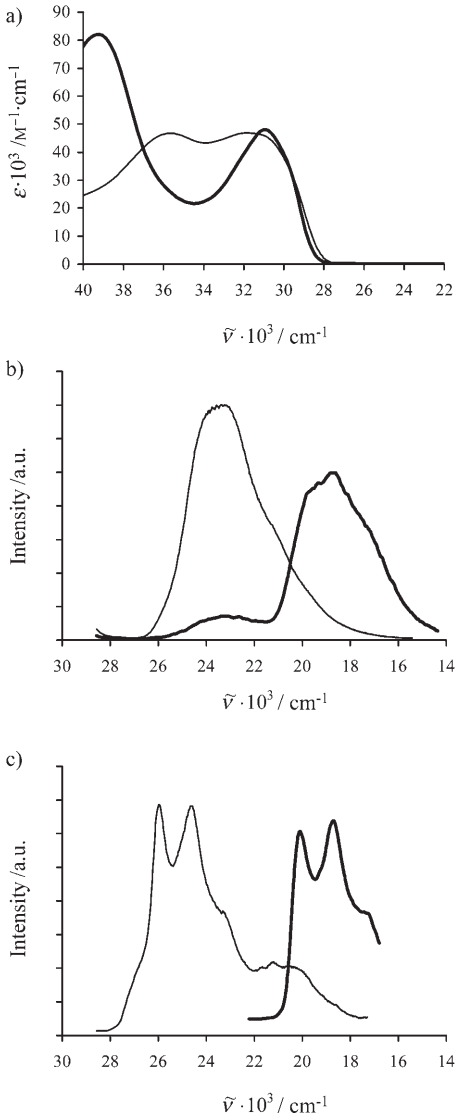

Figure 7. a) Absorption spectra of $\mathbf{L4}^{C12}$ (thin line) and $\mathbf{L5}^{C12}$ (bold line) in CH_2Cl_2/CH_3CN (1:1) at 298 K. b) Emission spectra of $\mathbf{L4}^{C12}$ at 77 K ($\tilde{\nu}_{exc}$ = 29240 cm^{-1}). Thin line = fluorescence, bold line = phosphorescence (delay time = 1 ms, intensity ×10). c) Emission spectra of $\mathbf{L5}^{C12}$ at 77 K ($\tilde{\nu}_{exc}$ = 29410 cm^{-1}). Thin line = fluorescence, bold line = phosphorescence (delay time = 1 ms, intensity ×10).

tals, in agreement with the electrostatic character of metal–ligand bonds in lanthanide complexes.[27] Therefore, the binding of $Lu(NO_3)_3$ to the ligand roughly corresponds to the connection of a strong electron-attractive substituent to the three coordinated nitrogen atoms. This produces a global decrease of about 1 eV in the energy of the orbitals centered on the tridentate binding unit on going from the free ligands $\mathbf{L}i$ (Figure 2) to the associated complexes $[Lu(\mathbf{L}i^{C1})(NO_3)_3]$ (Figure 5). On the other hand, the orbitals located on the appended phenyl rings are only marginally affected. Consequently, the HOMO (148a) and the occupied orbitals close to it (147a, 141b, 140b) are π orbitals centered on the appended phenyl rings, while the LUMO (142b) and SLUMO (149a) are centered on the central pyridine ring in $[Lu(\mathbf{L4}^{C1})(NO_3)_3]$ and in $[Lu(\mathbf{L5}^{C1})(NO_3)_3]$ (Figure 5), a situation previously encountered for **L5**, but not for **L4** in the free ligands (Figure 2). Consequently, the lowest allowed singlet–singlet electronic transitions possess strong phenyl(HOMO)→pyridine(LUMO) charge-transfer character, which strictly limits overlap density and oscillating strengths (Tables S12 and S13, Supporting Information). The lowest electronic transitions displaying significant intensities in the complexes thus involve the HOMO centered on the tridentate binding unit (146a in $[Lu(\mathbf{L4}^{C1})(NO_3)_3]$ and 145a in $[Lu(\mathbf{L5}^{C1})(NO_3)_3]$) and the LUMO centered on the pyridine ring (142b, Figure 5). The latter transition is predicted to occur at slightly lower energy for $[Lu(\mathbf{L4}^{C1})(NO_3)_3]$ than for $[Lu(\mathbf{L5}^{C1})(NO_3)_3]$ (ΔE = 1747 cm^{-1}), because of the inversion of the ester spacers; a trend previously found for the free ligands, and experimentally supported by the electronic absorption spectra of the complexes $[Lu(\mathbf{L}i^{C12})(NO_3)_3]$ (i = 4, 5; ΔE = 1320 cm^{-1} in CH_2Cl_2:CH_3CN (1:1), Table 5 and Figure 8a). Moreover, the electron-attracting effect of the bound $Lu(NO_3)_3$ core in the complexes reduces the energy of the lowest ligand-centered emissive $^1\pi\pi^*$ states (level 19

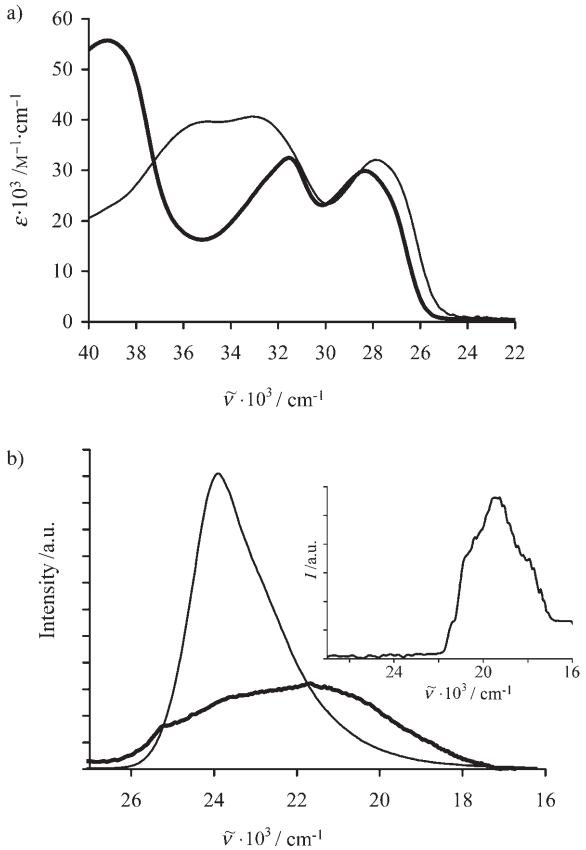

Figure 8. a) Absorption spectra of $[Lu(\mathbf{L4}^{C12})(NO_3)_3]$ (thin line) and $[Lu(\mathbf{L5}^{C12})(NO_3)_3]$ (bold line) in CH_2Cl_2/CH_3CN (1:1) at 298 K. b) Fluorescence spectra of $[Lu(\mathbf{L4}^{C12})(NO_3)_3]$ (thin line, $\tilde{\nu}_{exc}$ = 29410 cm^{-1}) and $[Lu(\mathbf{L5}^{C12})(NO_3)_3]$ (bold line, $\tilde{\nu}_{exc}$ = 30300 cm^{-1} intensity ×10) in the solid state at 298 K. The inset shows the phosphorescence spectrum of $[Lu(\mathbf{L5}^{C12})(NO_3)_3]$ at 77 K ($\tilde{\nu}_{exc}$ = 29080 cm^{-1}, delay time = 1 ms).

for $[Lu(\mathbf{L4}^{C1})(NO_3)_3]$ in Table S12 and level 28 for $[Lu(\mathbf{L5}^{C1})(NO_3)_3]$ in Table S13, Supporting Information), and we calculate red shifts of 4547 and 3125 cm^{-1} on going from the free ligands to the complexes. Experimental red shifts of 2800 and 1770 cm^{-1} are indeed observed in CH_2Cl_2/CH_3CN for the low-energy π–π^* transitions centered on the tridentate binding units on going from $\mathbf{L4}^{C12}$ to $[Lu(\mathbf{L4}^{C12})(NO_3)_3]$ and from $\mathbf{L5}^{C12}$ to $[Lu(\mathbf{L5}^{C12})(NO_3)_3]$ (Figures 7a and 8a; Table 5). Interestingly, the TD-DFT computed singlet–triplet energy gap between the two lowest excited states $^1\pi\pi^*$ and $^3\pi\pi^*$ is smaller for $\mathbf{L5}^{C1}$ ($\Delta E^{S-T}=E(^1\pi\pi^*$, level 3 in Table S5, Supporting Information$)-E(^3\pi\pi^*$, level 1 in Table S5$)=5\ cm^{-1}$, $[Lu(\mathbf{L5}^{C1})(NO_3)_3]$ ($\Delta E^{S-T}=75\ cm^{-1}$ calculated between the related electronic levels in Table S13, Supporting Information) and $[Lu(\mathbf{L4}^{C1})(NO_3)_3]$, ($\Delta E^{S-T}=E(^1\pi\pi^*$, level 3 in Table S12, Supporting Information$)-E(^3\pi\pi^*$, level 1 in Table S12, Supporting Information$)=220\ cm^{-1}$), than for $\mathbf{L4}^{C1}$ ($\Delta E^{S-T}=1970\ cm^{-1}$ calculated between the related electronic levels in Table S4). Since the reversal connection of the ester spacers on going from $\mathbf{L4}^{C1}$ to $\mathbf{L5}^{C1}$ or the complexation of $Ln(NO_3)_3$ to the ligands significantly decreases the energy of ligand-centered charge-transfer excited states, we expect a reduced overlap density of the two singly occupied orbitals in the triplet states of $\mathbf{L5}^{C1}$ (105a–106a in Figure 2 right), of $[Lu(\mathbf{L4}^{C1})(NO_3)_3]$ (148a–142b in Figure 5 left), and of $[Lu(\mathbf{L5}^{C1})(NO_3)_3]$ (148a–142b in Figure 5 right). This limits ΔE^{S-T} for these systems ($\Delta E^{S-T}=5$–$220\ cm^{-1}$), while the contrasting considerable overlap density existing between the related orbitals 105a and 103b in $\mathbf{L4}^{C1}$ (Figure 2, left) efficiently stabilizes the triplet state with respect to the singlet state ($\Delta E^{S-T}=1970\ cm^{-1}$), in complete agreement with a simple Heitler–London interpretation using the active-electron approximation.[25] For the open-shell $4f^7$ paramagnetic complexes $[Gd(\mathbf{L}\boldsymbol{i}^{C12})(NO_3)_3]$ ($i=4$, 5), in which no metal-centered excited levels are accessible for intramolecular energy transfers from the ligand-centered $^1\pi\pi^*$ or $^3\pi\pi^*$ levels,[28] we expect some improvements of 1) the $^1\pi\pi^*\rightarrow{}^3\pi\pi^*$ intersystem crossing process (isc) and 2) the oscillator strength of the spin-forbidden transition implying the $^3\pi\pi^*$ level because the Coulomb interactions between the electrons of the ligands and of the metal ions mix the ligand-centered triplet and singlet wavefunctions.[29] Surprisingly, these effects cannot be detected because the phosphorescence spectra of $[Gd(\mathbf{L}\boldsymbol{i}^{C12})(NO_3)_3]$ ($i=4$, 5) are dominated by the Eu- and Tb-centered emissions arising from traces ($<0.01\,\%$) of $[Eu(\mathbf{L}\boldsymbol{i}^{C12})(NO_3)_3]$ (detected at room temperature, Figure S11a, Supporting Information) and $[Tb(\mathbf{L}\boldsymbol{i}^{C12})(NO_3)_3]$ (detected below 77 K, Figure S11b, Supporting Information) in the "pure" ($>99.99\,\%$) Gd sample. This phenomenon, originally discovered and investigated in details for the parent complex [Gd(2,6-bis(1-methyl-benzimidazol-2-yl)pyridine)$(NO_3)_3$], results from the occurrence of extremely efficient, thermally activated, ligand-centered, energy-migration processes in the solid state, which are not perturbated by the appended aromatic side arms and by the ester spacers.[30]

Upon ligand-centered irradiation through the $\pi^*\leftarrow\pi$ transitions, the pure Eu^{III} complexes $[Eu(\mathbf{L}\boldsymbol{i}^{C12})(NO_3)_3]$ ($i=4$, 5) display standard $Eu(^5D_0\rightarrow{}^7F_J)$ ($J=0$–4) emission bands dominated by the hypersensitive electric dipolar $^5D_0\rightarrow{}^7F_2$ transition (Figure S12, Supporting Information). Both spectra are almost superimposable and correspond to the low-symmetry nine-coordinate EuN_3O_6 environment previously established for the anhydrous model complex [Eu(2,6-bis(1,1′-doctyl-benzimidazol-2-yl)pyridine)$(NO_3)_3$].[30] The $Eu(^5D_0)$ lifetime $\tau_{77K}^{Eu\text{-}\mathbf{L5}C12}=1.04(2)$ ms is monoexponential and fairly matches those found 1) for the model complex [Eu(2,6-bis(1-octyl-benzimidazol-2-yl)pyridine)$(NO_3)_3$] ($\tau=1.11$–1.15 ms, 4–295 K)[30] and 2) for the isomer $[Eu(\mathbf{L4}^{C12})(NO_3)_3]$ ($\tau^{Eu\text{-}\mathbf{L4}C12}=1.25$–1.29 ms, 10–295 K).[9d] We thus deduce that no OH oscillator (i.e., water molecule) lies in the first coordination sphere. Consequently, the sixfold decrease in quantum yields on going from $[Eu(\mathbf{L4}^{C12})(NO_3)_3]$ ($\Phi_{abs}=6(2)\,\%$) to $[Eu(\mathbf{L5}^{C12})(NO_3)_3]$ ($\Phi_{abs}=0.9(1)\,\%$) in acetonitrile/dichloromethane (1:1) can be safely assigned to the reverse connection of the ester spacers, which appear to slightly improve the sensitization process with $\mathbf{L4}^{C12}$. The analogous Tb^{III} complexes $[Tb(\mathbf{L}\boldsymbol{i}^{C12})(NO_3)_3]$ ($i=4$, 5) are poorly luminescent, because of efficient $Tb(^5D_4)\rightarrow\mathbf{L}\boldsymbol{i}(^3\pi\pi^*)$ thermally-activated energy back transfers operating between the almost two resonant levels, which dramatically quenches Tb^{III} emission at room temperature.[30] At 293 K in solution, we measure $\Phi_{abs}=0.6(4)\,\%$ for $[Tb(\mathbf{L4}^{C12})(NO_3)_3]$ and $\Phi_{abs}<0.1\,\%$ for $[Tb(\mathbf{L5}^{C12})(NO_3)_3]$.

Discussion

From a structural point of view, the opposite orientation of the ester spacers in $\mathbf{L4}^{Cn}$ and $\mathbf{L5}^{Cn}$ only affects the spatial arrangement of the carbonyl groups, which are coplanar with the aromatic rings to which they are connected (i.e., the terminal phenyl ring in $\mathbf{L4}^{Cn}$ and the benzimidazole ring in $\mathbf{L5}^{Cn}$). Except for the dimerization process occurring in solution with large Ln^{III} [Eq. (2)], which is enthalpically less favorable for $[Ln(\mathbf{L5}^{C12})(NO_3)_3]$ because of the presence of sterically demanding in-plane carbonyl groups, these minor geometrical changes have negligible structural consequences and the global cross-hatched organization of the appended phenyl rings with respect to the central planar 2,6-bis(benzimidazol-2-yl)pyridine is maintained in the ligands $\mathbf{L}\boldsymbol{i}^{Cn}$ and in their Ln^{III} complexes $[Ln(\mathbf{L}\boldsymbol{i}^{C12})(NO_3)_3]$ ($i=4$, 5). If these futile structural variations do not justify such detailed investigations, the changes in the electronic structure and their expression in the mesogenic and photophysical properties do bring novel tools for rationalizing and for programming functional metallomesogens. Firstly, the ester spacers act as ambivalent electron-attracting and electron-donating substituents for the aromatic rings, depending on their connection through their C or O atoms, respectively. Although, the ^1H NMR signals of the aromatic protons are dramatically affected by the orientation of the spacers, they cannot be used

as simple diagnostic probes for electron densities borne by the aromatic rings, because shielding or deshielding effects result from balances between inductive effect and through-space diamagnetic anisotropies associated with ring-current mechanisms.[23] However, sophisticated DFT calculations performed on optimized molecular structures in the gas phase show electrostatic potentials compatible with some simple predictions considering an O-bound ester as a donor group and a C-bound ester as an acceptor group (Scheme 1, Figures 3 and 6). When calculated on the Connolly surface of a molecule (ligand or complex), the electrostatic potential can be used as a guide for estimating the efficiency of π-stacking interactions occurring in condensed phases according to the rules of Sanders and Hunter: 1) π-stacking interactions are globally repulsive, 2) like polarizations repel and 3) opposite polarizations attract.[11] Following Nguyen's empirical suggestion,[12] we confirm here that the formation of mesophases is favored by an alternation of electron-poor and electron-rich π-systems along the rigid core, which helps in providing self-complementarity and strong cohesion in condensed phases. Such alternation exists for both $\mathbf{L4}^{C12}$ and $\mathbf{L5}^{C12}$, although the electrostatic potentials calculated in the gas phase indicate some leveling resulting from intramolecular polarization effects. We thus indeed observe comparable intermolecular π-stacking interactions in the crystals (each molecule is involved in four interactions) and the formation of similar hexagonal columnar mesophases close to room temperature. For the complexes $[Ln(\mathbf{L4}^{C12})(NO_3)_3]$ and $[Ln(\mathbf{L5}^{C12})(NO_3)_3]$, the strong electro-attractive polarization brought by the central trivalent lanthanide drastically decreases the electron density on the central tridentate binding unit, and consequently reduces the alternation between electron-rich and electron-poor aromatic rings along the strand. For $[Ln(\mathbf{L4}^{C12})(NO_3)_3]$, the connection of the ester spacers through their O-donor atoms to the benzimidazole rings partially overcomes the electron depletion in the six-membered ring of the coordinated benzimidazole, and mesomorphism is maintained (each rigid core of the complex is involved in six intermolecular π-stacking interactions in the solid state).[9d] For $[Ln(\mathbf{L5}^{C12})(NO_3)_3]$, the connection of the ester spacer through their attracting carbon atom further contributes to the depletion of the electronic density in the coordinated benzimidazole ring, and the alternation of polarization is reduced (each rigid core of the complex is involved in only four intermolecular π-stacking interactions in the solid state). No mesophase is detected, and $[Ln(\mathbf{L5}^{C12})(NO_3)_3]$ simply melt to give liquids. If we now consider potential exploitations of the photophysical properties brought into the mesophases by the Ln-centered luminescence,[31] the TD-DFT calculations show that the concentration of the donor substituents within the terminal phenyl rings in $\mathbf{L5}^{Cn}$ drastically reduces the HOMO–LUMO gap and puts the HOMO onto the appended aromatic rings. The experimental electronic absorption spectra of the systems with $\mathbf{L4}^{C12}$ and $\mathbf{L5}^{C12}$ are not very sensitive to this change, because only $\pi\rightarrow\pi^*$ transitions centered on the tridentate units possess enough oscillator strengths to be detected. However, the existence of a large amount of low-energy states in $\mathbf{L5}^{C12}$ provides efficient electronic relays favoring de-excitation processes, which significantly quenches the emission intensities in $\mathbf{L5}^{Cn}$ and in its complexes $[Ln(\mathbf{L5}^{C12})(NO_3)_3]$ (Ln = Eu, Gd, Tb, Lu).

Conclusion

The reversal connection of the ester spacers on going from $\mathbf{L4}^{Cn}$ to $\mathbf{L5}^{Cn}$ is harmful for both mesomorphism and luminescence. However, the investigation into the origin of this behavior allows us to propose some predictive rules for "rationally" designing luminescent thermotropic lanthanido-mesogens with this class of organic receptors.

1) The intermolecular cohesion forces between the polarizable aromatic cores, which are responsible for the microsegregation processes leading to the formation of the thermotropic mesophases, can be roughly estimated by considering the efficiency and the amount of packing interactions occurring in the solid state.
2) An alternance of a sufficient number of electron-rich and electron-poor aromatic rings along the rigid core favors efficient intermolecular interactions in condensed phases, which are partially maintained in the mesophases. This electrostatic effect can be, a priori, estimated by the electrostatic potential calculated on the Connolly surface of the molecule by DFT in the gas phase.
3) The ester spacers should be oriented in order to maximize the alternance between electron-rich and electron-poor aromatic rings along the strand.
4) The overall quantum yields of the Eu^{III} and Tb^{III} complexes strongly depend on the ligand-centered sensitization process, and it thus benefits from a large HOMO–LUMO gap, which is produced when low-energy charge-transfer states are avoided.

With the three first rules in mind, we can predict that the extended ligand $\mathbf{L6}^{C12}$ is a good candidate for restoring mesomorphism in the complexes $[Ln(\mathbf{L6}^{C12})(NO_3)_3]$, despite the "wrong" orientation of the ester groups, which previously appeared to be harmful for the formation of mesophases with $[Ln(\mathbf{L5}^{C12})(NO_3)_3]$. The major change on going from $\mathbf{L5}^{C12}$ to $\mathbf{L6}^{C12}$ concerns the introduction of an interstitial electron-rich *p*-diphenol ring in between two electron-poor aromatic moieties provided by the carbon connection of the ester spacers. This provides an alternance of nine aromatic portions with opposite polarizations along the strand in $\mathbf{L6}^{C12}$, and an alternance of five aromatic portions with opposite polarizations in $[Lu(\mathbf{L6}^{C12})(NO_3)_3]$ (Scheme 3), whereas only three related aromatic portions exist in $[Lu(\mathbf{L5}^{C12})(NO_3)_3]$ (Scheme 1). Preliminary DSC (Table 2) and SAXS studies (Table S8 and Figure S13, Supporting Information) indeed show that both the free ligand $\mathbf{L6}^{C12}$ and its complex $[Lu(\mathbf{L6}^{C12})(NO_3)_3]$ display hexagonal columnar mesophases (Col_h), while $[Lu(\mathbf{L5}^{C12})(NO_3)_3]$ simply melts to

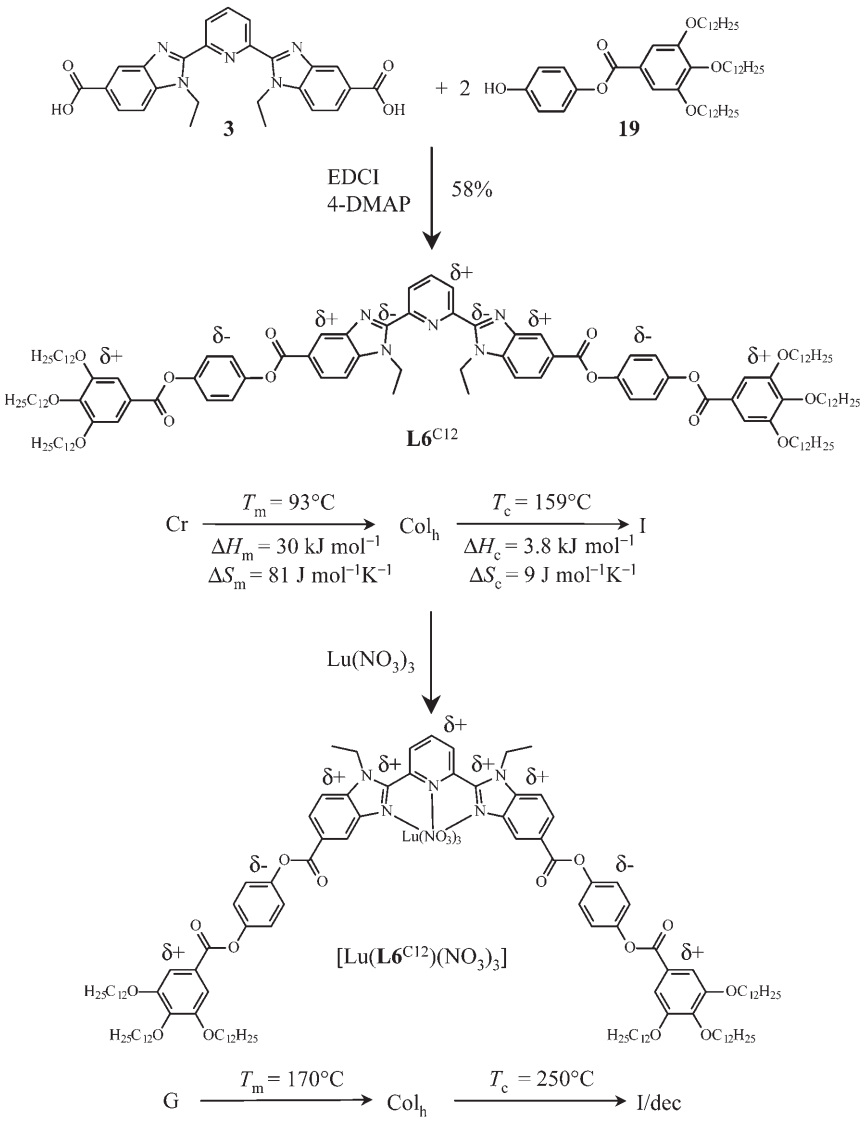

Scheme 3. Synthesis and mesomorphism of the extended ligand $\mathbf{L6}^{C12}$ and of its complex $[Lu(\mathbf{L6}^{C12})(NO_3)_3]$.

give a liquid. The transition temperatures observed for $\mathbf{L6}^{C12}$ and its complex $[Lu(\mathbf{L6}^{C12})(NO_3)_3]$ are slightly higher than those found for the related systems with $\mathbf{L5}^{C12}$ and $\mathbf{L4}^{C12}$,[9d] in agreement with the expected larger enthalpic contributions to the melting and clearing processes resulting from the improved sizes of the rigid cores. Finally, it is worth noting the considerable contraction of the lattice parameter a in the Col_h mesophase on going from $\mathbf{L6}^{C12}$ to its complex $[Lu(\mathbf{L6}^{C12})(NO_3)_3]$ (Table 2, and Table S8, Supporting Information), which reflects the change from rodlike→bent shapes occurring upon complexation of the ligand strand (Scheme 3).

We eventually conclude that the judicious design of aromatic rings with opposite polarization along the strand represents a novel and useful tool for chemically tuning the enthalpic contributions to the melting and clearing processes (ΔH_m^{chains} and ΔH_m^{cores}). However, the observation that $T_m([Lu(\mathbf{L4}^{C12})(NO_3)_3]) \approx T_m([Lu(\mathbf{L5}^{C12})(NO_3)_3])$, but $T_c([Lu(\mathbf{L4}^{C12})(NO_3)_3]) \gg T_m([Lu(\mathbf{L5}^{C12})(NO_3)_3])$ suggests that, among these two enthalpic contributions, ΔH_m^{cores} is more influenced by minor changes in intermolecular aromatic stacking interactions occurring in condensed phases. After having shown that ΔS_m^{chains} is the first thermodynamic parameter that can be rationally tuned for inducing mesomorphism in lanthanidomesogens with these systems,[9d] ΔH_m^{cores} represents a second opportunity for chemists to induce and to control the formation of mesophases in lanthanidomesogens, and probably more generally in metallomesogens.

Experimental Section

Solvents, starting materials and syntheses: Chemicals were purchased from Fluka AG and Aldrich, and used without further purification unless otherwise stated. The synthon 2,6-bis-(1-ethyl-5-methoxymethyl-benzimidazol-2-yl)pyridine (**1**) was prepared according to a literature procedure.[6] The nitrate salts $Ln(NO_3)_3{\cdot}xH_2O$ (Ln = La–Lu, Y, x = 1–4) were prepared from the corresponding oxides (Rhodia, 99.99%).[32] The Ln content of solid salts was determined by complexometric titrations with Titriplex III (Merck) in the presence of urotropine and xylene orange.[33] Acetonitrile and dichloromethane were distilled over calcium hydride, diethyl ether and tetrahydrofuran were distilled from sodium.

Preparation of 2,6-bis(1-ethyl-5-carboxybenzimidazol-2-yl)pyridinedimethyl ester (2): Compound **1** (1.06 g, 2.33 mmol), $KMnO_4$ (7.35 g, 46.54 mmol), and triethylbenzylammonium chloride (10.60 g, 46.54 mmol) were refluxed in dichloromethane (100 mL) for 3 d. Excess $KMnO_4$ was removed by addition of a concentrated aqueous solution of $Na_2S_2O_5$ until the complete disappearance of the violet color. The organic phase was separated and the aqueous phase was extracted with dichloromethane (3×100 mL). The combined organic phases were dried (Na_2SO_4), filtered, and evaporated to dryness. The crude yellow residue was purified by column chromatography (silica gel; CH_2Cl_2/MeOH 99.5:0.5→99:1) to give 0.8 g (1.63 mmol, yield 71%) of **2** as a microcrystalline white solid. ^{1}H NMR ($CDCl_3$): δ = 1.35 (t, J^3 = 7.5 Hz, 6H), 3.94 (s, 6H), 4.78 (q, J^3 = 6.9 Hz, 4H), 7.47 (d, J^3 = 8.7 Hz, 2H), 8.07 (dd, J^3 = 8.7 Hz, J^4 = 1.5 Hz, 2H), 8.07 (t, J^3 = 7.8 Hz, 1H), 8.36 (d, J^3 = 7.8 Hz, 2H), 8.56 ppm (d, J^4 = 1.2 Hz, 2H); ^{13}C NMR ([D$_6$]DMSO): δ = 15.66, 52.40 (C_{prim}); 40.33 (C_{sec}); 110.17, 123.00, 125.26, 126.46, 138.63 (C_{tert}); 139.31, 142.62, 149.83, 151.61, 167.70 ppm (C_{quat}); ESI-MS (CH_2Cl_2/MeOH 9:1): m/z: 506.2 $[M+Na]^+$, 989.4 $[2M+Na]^+$; recrystallization from acetonitrile gave X-ray quality prisms of **2**.

Preparation of 2,6-bis-(1-ethyl-5-carboxybenzimidazol-2-yl)pyridine (3): Compound **2** (0.40 g, 0.83 mmol) and KOH (1.00 g, 17.82 mmol) were refluxed in ethanol/water (50 mL:20 mL) for 45 min. The hot solution was neutralized with conc. hydrochloric acid (35%) until pH 1.0, and a white precipitate formed upon cooling. The precipitate was filtered and dried under vacuum (90°C) to give 0.38 g (0.83 mmol, yield 100%) of **3** as a white solid. ^{1}H NMR ([D$_6$]DMSO): δ=1.29 (t, J^3=7 Hz, 6H), 4.82 (q, J^3=7 Hz, 4H), 7.84 (d, J^3=7 Hz, 2H), 7.96 (dd, J^3=8 Hz, J^4=1 Hz, 2H), 8.22–8.35 (m, 3H), 8.40 ppm (d, J^3=8 Hz, 2H); ^{13}C NMR ([D$_6$]DMSO): δ=15.64 (C$_{prim}$); 40.47 (C$_{sec}$); 111.76, 122.15, 125.12, 126.78, 139.59 (C$_{tert}$); 125.94, 139.53, 142.53, 149.84, 151.72, 168.35 ppm (C$_{quat}$); EI-MS: m/z: 455 $[M]^+$.

Preparation of 3,4,5-trialkoxybenzyl methyl ester (4^{Cn}, n=1, 12): Compound **4**^{C0} (8.00 g, 43.4 mmol), anhydrous potassium carbonate (54.17 g, 391.9 mmol), 1-bromododecane (38.37 g, 130.3 mmol) and potassium iodide (200 mg, 1.20 mmol) were refluxed in dry acetone (300 mL) for 2 d. The solution was evaporated to dryness, partitioned between dichloromethane (200 mL) and water (200 mL). The organic layer was separated, and the aqueous phase extracted with dichloromethane (3× 200 mL). The combined organic phases were dried (Na_2SO_4), filtered, and evaporated to give a colorless oil, which was triturated with ethanol (50 mL). The resulting voluminous white solid residue was filtered and dried under vacuum to give 15.27 g (22.15 mmol, yield 51%) of **4**^{C12} as a white solid. M.p.=45°C; ^{1}H NMR ($CDCl_3$): δ=0.91 (t, J^3=7 Hz, 18H), 1.24–1.42 (m, 48H), 1.46–1.53 (m, 6H), 1.75–1.87 (m, 6H), 3.91 (s, 3H), 4.02–4.05 (m, 6H), 7.27 ppm (s, 2H); ^{13}C NMR ($CDCl_3$): δ=14.11 , 50.09 (C$_{prim}$); 22.70 , 26.08, 26.10, 29.34, 29.37, 29.41, 29.58, 29.65, 29.67, 29.71, 29.74, 29.76, 30.35, 31.94, 31.95, 69.22, 73.51 (C$_{sec}$); 108.08 (C$_{tert}$); 124.67, 142.46, 152.84, 166.95 ppm (C$_{quat}$); EI-MS: m/z: 688 $[M]^+$. The same procedure was followed for the derivative **4**^{C1} by using methyliodide as the alkylating agent.

Data for 4^{C1}: ^{1}H NMR ($CDCl_3$): δ=3.88 (s, 9H), 3.91 (s, 3H), 7.33 ppm (s, 2H); ^{13}C NMR ($CDCl_3$): δ=56.42, 61.14 (C$_{prim}$); 107.56 (C$_{tert}$); 124.32, 143.13, 153.14, 166.95 ppm (C$_{quat}$); EI-MS: m/z: 226 $[M^+]$.

Preparation of 2-(3,4,5-trisdodecyloxyphenyl)propan-2-ol (5^{Cn}, n=0, 1, 12): Methyl iodide (2,27 g, 16.00 mmol) was added to a suspension of magnesium (0.39 g, 16.00 mmol) in dry diethyl ether (50 mL). The reaction was initiated by heating and then the temperature was controlled with a water/ice bath. When solid magnesium had disappeared, a solution of compound **4**^{C12} (5.00 g, 7.26 mmol) in dry diethyl ether (5 mL) was slowly added. The resulting mixture was refluxed for 12 h. Addition of a saturated aqueous ammonium chloride solution (10 mL) produced a vigorous reaction, then water (150 mL) and diethyl ether (150 mL) were added. The organic layer was separated, and the aqueous phase extracted with diethyl ether (3×50 mL). The combined organic phases were dried (Na_2SO_4), filtered, and evaporated to give a pale yellow oil. Column chromatography (silica gel; CH_2Cl_2) gave 4.50 g (6.53 mmol, yield 90%) of **5**^{C12} as a colorless oil, which was poorly stable at RT. ^{1}H NMR ($CDCl_3$): δ=0.91 (t, J^3=6.9 Hz, 18H), 1.23–1.39 (m, 48H), 1.45–1.53 (m, 6H), 1.58 (s, 6H), 1.73–1.85 (m, 6H), 3.96 (t, J^3=6.6 Hz, 2H), 4.01 (t, J^3=6.5 Hz, 4H), 6.70 ppm (s, 2H); EI-MS: m/z: 670 $[M^+]$. The same procedure was followed for the derivatives **5**^{C1} and **5**^{C0}.

Data for 5^{C1}: ^{1}H NMR ($CDCl_3$): δ=1.59 (s, 6H), 3.78 (s, 9H), 6.70 ppm (s, 2H); EI-MS: m/z: 208 $[M^+]$.

Data for 5^{C0}: ^{1}H NMR ($CDCl_3$): δ=1.60 (s, 6H), 6.72 ppm (s, 2H); EI-MS: m/z: 166 $[M^+]$.

Preparation of 3,4,5-trisdodecyloxyphenol (6^{Cn} , n=0, 1, 12): BF_3·Et_2O (2.06 g, 14.50 mmol) and $NaBO_3$·$4H_2O$ (0.45 g, 2.90 mmol) were dissolved in dry THF (20 mL) at 0°C. After 30 min stirring at 0°C, a solution of compound **5**^{C12} (1.00 g, 1.45 mmol) in THF (5 mL) was added and the reaction was left to reach RT, and stirred for a further 12 h. A saturated aqueous sodium sulfite solution (10 mL) was added together with water (100 mL). The resulting mixture was extracted with diethyl ether (3× 100 mL). The combined organic phases were dried (Na_2SO_4), filtered, and evaporated to give a brownish solid. Column chromatography (silica gel; CH_2Cl_2) gave 0.76 g (1.17 mmol, yield 81%) of **6**^{C12} as a air-sensitive pale yellow solid. M.p.=48°C; ^{1}H NMR ($CDCl_3$): δ_H 0.90 (t, J^3=6.9 Hz, 18H), 1.28–1.34 (m, 48H), 1.42–1.46 (m ,6H), 1.70–1.82 (m, 6H), 3.86–3.91 (m, 6H), 5.17 (m, 1H), 6.05 ppm (s, 2H); ^{13}C NMR ($CDCl_3$): δ=14.14 (C$_{prim}$); 22.73, 26.12, 26.18, 29.36, 29.41, 29.43, 29.46, 29.67, 29.69, 29.74, 29.77, 29.79, 30.27, 31.75, 31.96, 68.98, 73.69 (C$_{sec}$); 94.25 (C$_{tert}$); 131.89, 151.89, 153.54 ppm (C$_{quat}$); EI-MS: m/z: 647 $[M]^+$. The same procedure was followed for the derivatives **6**^{C1} and **6**^{C0}.

Data for 6^{C1}: ^{1}H NMR ($CDCl_3$): δ=3.70 (s, 9H), 5.25 (br s, 1H), 6.05 ppm (s, 2H); ^{13}C NMR ($CDCl_3$): δ=56.30 (C$_{prim}$); 94.10 (C$_{tert}$); 132.10, 151.65, 154.20 (C$_{quat}$); EI-MS: m/z: 185 [M$_+$].

Data for 6^{C0}: ^{1}H NMR ($CDCl_3$): δ=5.40 (br s, 4H), 6.12 ppm (s, 2H); EI-MS: m/z: 143 $[M^+]$.

Preparation of 2,6-bis-(1-ethyl-5-carboxybenzimidazol-2-yl)pyridine-di[3,4,5-tris(alkyloxy)benzyl] ester (L5^{Cn}; n=0, 1, 12): A catalytic amount of 4-dimethylaminopyridine, compound **3** (0.21 g, 0.46 mmol), compound **6**^{C12} (0.60 g, 0.93 mmol), and EDCI (0.36 g, 1.85 mmol) were refluxed for 6 h in CH_2Cl_2 (50 mL) under an inert atmosphere. The resulting mixture was washed with water (4×100 mL). The organic layer was separated, dried (Na_2SO_4), and evaporated to dryness. The crude yellow oil was purified by column chromatography (silica gel; CH_2Cl_2/MeOH 100:0→99:1) to give 0.56 g (0.33 mmol, yield 71%) of **L5**^{C12} as a pale yellow solid. ^{1}H NMR ($CDCl_3$): δ=0.82–0.86 (m, 18H), 1.23–1.40 (m, 114H), 1.69–1.86 (m, 12H), 3.91–3.96 (m, 12H), 4.83 (q, J^3=7.2 Hz, 4H), 6.45 (s, 4H), 7.54 (d, J^3=8.7 Hz, 2H), 8.10 (t, J^3=7.8 Hz, 1H), 8.20 (dd, J^3=8.7 Hz, J^4=1.5 Hz, 2H), 8.40 (d, J^3=7.8 Hz, 2H), 8.72 ppm (d, J^4=1.5 Hz, 2H); ^{13}C NMR ($CDCl_3$): δ=14.32, 15.69 (C$_{prim}$); 14.32, 15.69, 22.89, 26.29, 26.36, 29.50, 29.57, 29.61, 29.85, 29.90, 29.98, 30.55, 32.13, 32.15, 40.43, 69.31, 73.73 (C$_{sec}$); 100.54, 110.37, 123.73, 125.69, 126.59, 138.69 (C$_{tert}$); 124.60, 136.03, 139.76, 142.75, 146.95, 149.82, 151.85, 153.57, 165.88 ppm (C$_{quat}$); ESI-MS (CH_2Cl_2/MeOH 9:1 + HCl 0.1%): m/z: 1714.4 $[M+H]^+$; elemental analysis calcd (%) for $C_{109}H_{173}N_5O_{10}$·$0.6H_2O$ (1724.40): C 75.90, H 10.10, N 4.06; found: C 75.61, H 10.26, N 3.94; the same procedure was followed for the ligands **L5**^{C1} and **L5**^{C0}.

Data for L5^{C1}: ^{1}H NMR ($CDCl_3$): δ=1.39 (t, J^3=7.2 Hz, 6H), 3.85 (s, 18H), 4.84 (q, J^3=6.7 Hz, 4H), 6.50 (s, 4H), 7.55 (d, J^3=8.7 Hz, 2H), 8.10 (t, J^3=7.8 Hz, 1H), 8.20 (dd, J^3=8.7 Hz, J^4=1.5 Hz, 2H), 8.40 (d, J^3=7.8 Hz, 2H), 8.73 ppm (d, J^4=1.5 Hz, 2H); ^{13}C NMR ($CDCl_3$): δ=15.68, 56.39, 61.15 (C$_{prim}$); 40.44 (C$_{sec}$); 99.58, 110.42, 123.76, 125.70, 126.61, 138.68 (C$_{tert}$); 124.41, 136.05, 139.84, 142.78, 147.43, 149.82, 151.89, 153.77, 165.87 ppm (C$_{quat}$); ESI-MS (CH_2Cl_2/MeOH 9:1): m/z: 810.3 $[M+Na]^+$, 1598.2 $[2M+Na]^+$; elemental analysis calcd (%) for $C_{43}H_{41}N_5O_{10}$·$0.6H_2O$ (798.62): C 64.67, H 5.33, N 8.77; found: C 64.70, H 5.41, N 8.77; recrystallization from CH_2Cl_2/hexane gave X-ray quality prisms of **L5**^{C12}·$0.5CH_2Cl_2$.

Data for L5^{C0}: ^{1}H NMR ($CDCl_3$): δ=1.45 (t, J^3=7.2 Hz, 6H), 4.90 (q, J^3=7.2 Hz, 4H), 7.28–7.40 (m, 6H), 7.47–7.51 (m, 4H), 7.62 (d, J^3=8.6 Hz, 2H), 8.17 (t, J^3=7.9 Hz, 1H), 8.29 (dd, J^3=8.6 Hz, J^4=1.6 Hz, 2H), 8.48 (d, J^3=7.9 Hz, 2H), 8.82 ppm (d, J^4=1.3 Hz, 2H); ^{13}C NMR ($CDCl_3$): δ=15.51 (C$_{prim}$); 40.32 (C$_{sec}$); 110.30, 121.83, 123.48, 125.68, 125.85, 126.57, 138.59 (C$_{tert}$); 124.56, 139.48, 151.19, 151.53, 165.53 ppm (C$_{quat}$); ESI-MS (CH_2Cl_2/MeOH 9:1): m/z: 608.2 $[M]^+$, 630.2 $[M+Na]^+$, 1214.2 $[2M]^+$, 1237.2 $[2M+Na]^+$; elemental analysis calcd (%) for $C_{37}H_{29}N_5O_4$ (607.67): C 73.13, H 4.81, N 11.52; found: C 73.23, H 4.71, N 11.56.

Preparation of (4-hydroxyphenyl)-1-(3,4,5-trimethoxy)benzoic acid ester (19): A catalytic amount of 4-dimethylaminopyridine, 3,4,5-tri(dodecyloxy)benzoic acid (3.00 g, 4.44 mmol),[9d] 4-benzyloxyphenol (0.82 g, 4.10 mmol), and dicyclohexylcarbodiimide (DCC, 1.83 g, 8.87 mmol) were refluxed for 16 h in CH_2Cl_2 (100 mL). The resulting insoluble dicyclohexylurea was separated by filtration and the resulting mixture evaporated to dryness. The colorless oil was purified by column chromatography (silica gel; CH_2Cl_2), then recrystallized from ethanol to give 3.29 g (3.84 mmol, yield 84%) of (*p*-benzyloxyphenyl)-1-(3,4,5-trimethoxy)benzoic acid ester as a white solid. M.p.=43°C; ^{1}H NMR ($CDCl_3$): δ=0.85 (t, J^3=6.9 Hz, 9H), 1.15–1.60 (m, 54H), 1.68–1.84 (m, 6H), 3.98–4.04 (m, 6H), 5.05 (s, 2H), 6.98 (d, J^3=9.3 Hz, 2H), 7.08 (t, J^3=9.3 Hz, 2H), 7.28–7.44 ppm (m, 7H); ^{13}C NMR ($CDCl_3$): δ=14.43 (C$_{prim}$); 22.91, 26.29, 29.49, 29.58, 29.61, 29.79, 29.85, 29.87, 29.91, 29.94, 30.55, 32.14, 69.41, 70.61, 73.77 (C$_{sec}$); 108.65, 115.70, 122.75, 127.70, 128.24, 128.82 (C$_{tert}$);

124.18, 137.02, 143.05, 144.87, 153.13, 156.68, 165.58 ppm (C_{quat}); EI-MS : m/z: 857 $[M]^+$. (*p*-Benzyloxyphenyl)-1-(3,4,5-trimethoxy)benzoic acid ester (2.08 g, 2.43 mmol) was then dissolved in a solution containing a suspension of Pd/C (0.10 g, 10%) in CH_2Cl_2:CH_3OH (100 mL:10 mL). The mixture was refluxed at RT under dihydrogen (1 bar) for one hour. Filtration over Celite, followed by evaporation, and drying under vacuum gave 1.85 g (2.41 mmol, yield 99%) of **19** as a white solid. M.p. = 59 °C; ^{1}H NMR ($CDCl_3$): $\delta = 0.84$ (t, $J^3 = 6.9$ Hz, 9H), 1.15–1.60 (m, 54H), 1.70–1.82 (m, 6H), 3.97–4.04 (m, 6H), 4.77 (s, 1H), 6.82 (d, $J^3 = 8.7$ Hz, 2H), 7.01 (d, $J^3 = 8.7$ Hz, 2H), 7.35 ppm (s, 2H); ^{13}C NMR ($CDCl_3$): $\delta = 14.34$ (C_{prim}); 22.91, 26.29, 29.48, 29.58, 29.61, 29.78, 29.85, 29.87, 29.91, 29.95, 30.52, 32.14, 69.42, 73.83 (C_{sec}); 108.64, 116.38, 122.78 (C_{tert}); 124.06, 143.05, 144.49, 153.13, 153.74, 166.09 ppm (C_{quat}); EI-MS : m/z: 767 $[M]^+$.

Preparation of 2,6-bis-(1-ethyl-5-carboxybenzimidazol-2-yl)pyridine-di(3,4,5-trimethoxybenzoic acid 4-hydroxyphenyl ester) ester ($\mathbf{L6}^{C12}$): A catalytic amount of 4-dimethylaminopyridine, compound **3** (0.30 g, 0.66 mmol), compound **19** (1.00 g, 1.30 mmol), and EDCI (1.01 g, 5.21 mmol) were refluxed for 12 h in CH_2Cl_2 (100 mL) under an inert atmosphere. The resulting mixture was washed with water (3×100 mL). The organic layer was separated, dried (Na_2SO_4), and evaporated to dryness. The crude yellow oil was purified by column chromatography (silica gel; CH_2Cl_2/MeOH 99.8:0.2→99:1) to give 0.75 g (0.38 mmol, yield 58%) of $\mathbf{L6}^{C12}$ as a white solid. ^{1}H NMR ($CDCl_3$): $\delta = 0.85$ (t, $J^3 = 6.6$ Hz, 18H), 1.15–1.55 (m, 108H), 1.40 (t, $J^3 = 7.2$ Hz, 6H), 1.69–1.90 (m, 12H), 4.01–4.05 (m, 12H), 4.84 (q, $J^3 = 6.9$ Hz, 4H), 7.25 (d, $J^3 = 9.0$ Hz, 4H), 7.32 (d, $J^3 = 9.0$ Hz, 4H), 7.39 (s, 4H), 7.56 (d, $J^3 = 8.7$ Hz, 2H), 8.11 (t, $J^3 = 8.1$ Hz, 1H), 8.23 (dd, $J^3 = 8.7$ Hz, $J^4 = 1.2$ Hz, 2H), 8.41 (d, $J^3 = 7.8$ Hz, 2H), 8.76 ppm (m, 2H); ^{13}C NMR ($CDCl_3$): δ_C 14.33, 15.71 (C_{prim}); 22.90, 26.28, 26.30, 29.51, 29.58, 29.61, 29.79, 29.85, 29.87, 29.92, 29.95, 30.56, 32.14, 40.46, 69.46, 73.79 (C_{sec}); 108.74, 110.47, 122.91, 123.78, 125.77, 126.64, 138.72 (C_{tert}); 123.95, 124.36, 139.84, 142.72, 143.23, 148.65, 148.78, 149.79, 151.88, 153.18, 165.17, 165.63 ppm ($C_{quat.}$); ESI-MS (CH_2Cl_2/MeOH 8:2 + HCl 0.1%): m/z: 1953.9 $[M+H]^+$; elemental analysis calcd (%) for $C_{123}H_{181}N_5O_{14}\cdot 1.57\,H_2O$ (1982.06): C 74.54, H 9.36, N 3.53; found: C 74.54, H 9.41, N 3.45.

Preparation of the complexes [Ln($\mathbf{L5}^{C12}$)$(NO_3)_3$] (Ln = Sm-Lu): A solution of compound $\mathbf{L5}^{C12}$ (0.1 g, 5.84×10^{-5} mol) in dichloromethane (5 mL) was added to $Ln(NO_3)_3\cdot x\,H_2O$ (Ln = Sm–Lu, x = 2–4) in acetonitrile (5 mL). After 1 h stirring at RT, the dichloromethane was evaporated, the solution was cooled to −20 °C, and the white precipitate was filtered, washed with CH_3CN, and dried to give 80% of [Ln($\mathbf{L5}^{C12}$)$(NO_3)_3$]·$n\,H_2O$ (Ln = Sm, n = 3.5, **7**; Ln = Eu, n = 2.5, **8**; Ln = Gd, n = 3, **9**; Ln = Tb, n = 0, **10**; Ln = Dy, n = 0, **11**; Ln = Ho, n = 1.5, **12**; Ln = Er, n = 0, **13**; Ln = Tm, n = 1, **14**; Ln = Yb, n = 0.5, **15**; Ln = Lu, n = 1.5, **16**). All the complexes were characterized by satisfying elemental analyses (Table S9, Supporting Information) and IR spectra. X-ray quality prisms of [Eu(**2**)$(NO_3)_3(H_2O)$](CH_3NO_2) (**17**) and [Yb($\mathbf{L5}^{C0}$)$(NO_3)_3$]$(CH_3CN)_2$ (**18**) were obtained by slow diffusion of diethyl ether into concentrated solutions of the complexes in nitromethane and acetonitrile, respectively.

Single crystal structure determinations: Summary of crystal data, intensity measurements and structure refinements for **2**, $\mathbf{L5}^{C1}\cdot 0.5CH_2Cl_2$, [Eu(**2**)$(NO_3)_3(H_2O)$]$(CH_3NO_2)$ (**17**) and [Yb($\mathbf{L5}^{C0}$)$(NO_3)_3$]$(CH_3CN)_2$ (**18**) are collected in Table S16 (Supporting Information). All crystals were mounted on quartz fibers with protection oil. Cell dimensions and intensities were measured at 200 K on a Stoe IPDS diffractometer with graphite-monochromated $Mo_{K\alpha}$ radiation ($\lambda = 0.71073$ Å). Data were corrected for Lorentz and polarization effects and for absorption. The structures were solved by direct methods (SIR97),[34] all other calculations were performed with the XTAL[35] system and ORTEP[36] programs. CCDC-611681–611684 (**2**, $\mathbf{L5}^{C1}\cdot 0.5CH_2Cl_2$, [Eu(**2**)$(NO_3)_3(H_2O)$]$(CH_3NO_2)$ (**17**) and [Yb($\mathbf{L5}^{C0}$)$(NO_3)_3$]$(CH_3CN)_2$ (**18**) respectively) contain the supplementary crystallographic data for this paper. These data can be obtained free of charge from The Cambridge Crystallographic Data Centre via www.ccdc.cam.ac.uk/data_request/cif.

In **2** and **17**, the hydrogen atoms were observed and refined with U_{iso} = 0.04 Å^2. The atomic positions of the other hydrogen atoms were calculated. For **2**, the ligand was located on a twofold axis with N1 and C3 in special position (*4e*). The CH_2Cl_2 molecule in $\mathbf{L5}^{C1}\cdot 0.5\,CH_2Cl_2$ was disordered about an inversion center and was refined with a population parameter of 0.5. In **17**, the hydrogen atoms of the methyl group of the nitromethane molecule were refined with restraints on bond lengths and bond angles.

Spectroscopic and analytical measurements: Electronic spectra in the UV/Vis region were recorded at 20 °C from solutions in CH_3CN/CH_2Cl_2 (1:1) with a Perkin–Elmer Lambda 900 spectrometer using quartz cells of 0.1 and 1 mm path length. Spectrophotometric titrations were performed with a J&M diode array spectrometer (Tidas series) connected to an external computer. In a typical experiment, $\mathbf{L5}^{C12}$ in CH_3CN/CH_2Cl_2 (1:1; 50 mL, $2\cdot10^{-4}$ mol dm^{-3}) were titrated at 20 °C with a solution of $Ln(NO_3)_3\cdot x H_2O$ (10^{-3} mol dm^{-3}) in the same solvent under an inert atmosphere. After each addition of 0.10 mL, the absorbance was recorded using Hellma optrodes (optical path length 0.1 cm) immersed in the thermostated titration vessel and connected to the spectrometer. Mathematical treatment of the spectrophotometric data was performed with factor analysis[37] and with the SPECFIT program.[33] IR spectra were obtained from KBr pellets with a FT-IR Perkin–Elmer Spectrum One. ^{1}H and ^{13}C NMR spectra were recorded at 25 °C on a Bruker Avance 400 MHz and Bruker DRX-500 MHz spectrometers. Chemical shifts are given in ppm with respect to TMS. Diffusion experiments were recorded at 400 MHz-proton-Larmor frequency at RT. The sequence corresponds to Bruker pulse program ledbpgp2s[38] by using stimulated echo, bipolar gradients and longitudinal eddy current delay as z filter. The four 2 ms gradients pulses have sine-bell shapes and amplitudes ranging linearly from 2.5 to 50 G cm^{-1} in 16 steps. The diffusion delay was 100 ms and the number of scans was 16. The processing was done by using a line broadening of 5 Hz and the diffusion rates were calculated by using the Bruker processing package. Pneumatically assisted electrospray (ESI-MS) mass spectra were recorded from 10^{-4} mol dm^{-3} solutions on a Finnigan SSQ7000 instrument. Quantum yields were determined using a Perkin–Elmer LS50B fluorimeter. The quantum yields were calculated using the equation $\frac{\Phi_x}{\Phi_r} = \frac{A_r(\tilde{\nu})I_r(\tilde{\nu})n_x^2 D_x}{A_x(\tilde{\nu})I_x(\tilde{\nu})n_r^2 D_r}$, in which x refers to the sample and r to the reference; A is the absorbance, $\tilde{\nu}$ the excitation wavenumber used, I the intensity of the excitation light at this energy, n the refractive index (n = 1.341 for acetonitrile solution and n = 1.330 for 0.1 mol dm^{-3} aqueous tris-buffer solution) and D the integrated emitted intensity. Cs_3[Eu(2,6-pyridinedicarboxylic acid)$_3$] (φ = 9.5% in 0.1 mol dm^{-3} aqueous tris-buffer solution) was used as reference.[39] TG were performed with a thermogravimetric balance Seiko TG/DTA 320 (under N_2). DSC traces were obtained with a Seiko DSC 220C differential scanning calorimeter from 3–5 mg samples (5 °C min^{-1}, under N_2). The characterization of the mesophases were performed with a polarizing microscope Leitz Orthoplan-Pol with a Leitz LL 20×/0.40 polarizing objective, and equipped with a Linkam THMS 600 variable-temperature stage. The SAXS patterns were obtained with two different experimental setups, and in all cases, the crude powder was filled in Lindemann capillaries of 1 mm diameter. The characterization of the wide-angle region and the measurements of the periodicities were achieved using a linear monochromatic $Cu_{K\alpha}$ beam obtained with a sealed-tube generator (900 W) and a bent quartz monochromator. One set of diffraction patterns was registered with a curved counter Inel CPS 120, for which the sample temperature was controlled within ±0.05 °C; periodicities up to 60 Å could be measured. The other set of diffraction patterns was registered on an image plate; the cell parameters were calculated from the position of the reflection at the smallest Bragg angle, which was in all cases the most intense. Periodicities up to 90 Å could be measured, and the sample temperature was controlled within ±0.3 °C. The exposure times were varied from 1 to 24 h depending on the specific reflections being sought (weaker reflections obviously taking longer exposure times). Elemental analyses were performed by Dr. H. Eder from the microchemical Laboratory of the University of Geneva.

Computational details: The geometries of ligands $\mathbf{L4}^{C1}$, $\mathbf{L5}^{C1}$ and complexes [Lu($\mathbf{L4}^{C1}$)$(NO_3)_3$] and [Lu($\mathbf{L5}^{C1}$)$(NO_3)_3$] were fully optimized at the DFT level using the B3LYP[40] hybrid functional as implemented in the Gaussian 03 package.[41] The crystal structures of $\mathbf{L4}^{C1}$,[9d] $\mathbf{L5}^{C1}$, [Yb($\mathbf{L4}^{C0}$)$(NO_3)_3$][9d] and [Yb($\mathbf{L5}^{C0}$)$(NO_3)_3$] were used as starting structural models and geometry optimizations were restricted to the C_2 sym-

metry point group. For all Gaussian 03 calculations, DZVP double-ζ basis set developed by Godbout and co-workers[42] was used for the H, C, and O atoms and the lutetium cation was described by the quasi-relativistic pseudopotential of Dolg and co-workers[43] for the 46 + 4f^n core electrons and by a (7 s, 6p, 5d)/(5 s, 4p, 3d) Gaussian basis set for the valence electrons. Fitted atomic charges were calculated according to the Merz–Singh–Kollmann scheme[18] using 25 points per layer. Connolly surfaces were generated using Molekel 4.3[44] and were then used to calculate molecular electrostatic potential (MEP). TD-DFT calculations of singlet–singlet and singlet–triplet excitation energies[45] were performed by using the Amsterdam density functional program (ADF 2005.01).[46] A Slater-type orbitals TZ2P all-electron basis set (double-ζ in core, triple-ζ in the valence region + 2 polarization functions) was used and relativistic effects were introduced using the Zero Order Regular Approximation (ZORA) formalism.[47] To ensure a correct asymptotic behavior to the exchange-correlation potential, the Statistical Average of Orbital Potential (SAOP)[48] was chosen for the TD-DFT calculations.

Acknowledgements

We thank H. Lartigue, K.-L. Buchwalder and B. Bocquet for their technical assistance and Dr T. Wesolowski for fruitful discussions. Financial support from the Swiss National Science Foundation is gratefully acknowledged.

[1] "Thermotropic Liquid Crystals": K. J. Toyne, *Crit. Rep. Appl. Chem.* **1987**, *22*, 28–63.

[2] a) D. Guillon, A. Skoulios, *J. Phys.* **1976**, *37*, 797–800; b) E. Terazzi, S. Suarez, S. Torelli, H. Nozary, D. Imbert, O. Mamula, J.-P. Rivera, E. Guillet, J.-M. Bénech, G. Bernardinelli, R. Scopelliti, B. Donnio, D. Guillon, J.-C. G. Bünzli, C. Piguet, *Adv. Funct. Mater.* **2006**, *16*, 157–168; c) C. Piguet, J.-C. G. Bünzli, B. Donnio, D. Guillon, *Chem. Commun.* **2006**, 3755–3768.

[3] a) J. L. Serrano, *Metallomesogens, Synthesis, Properties and Applications*, VCH, Weinheim, **1996**; b) B. Donnio, D. Guillon, R. Deschenaux, D. W. Bruce, in *Comprehensive Coordination Chemistry, Vol. 7* (Eds.: J. A. McCleverty, T. J. Meyer), Elsevier, Oxford (UK), **2003**, Chapter 7.9, pp. 357–627; c) R. Deschenaux, J. W. Goodby, in *Ferrocene: Homogeneous Catalysis, Organic Synthesis, Material Sciences* (Eds.: A. Togni, T. Hayashi), VCH, Weinheim (Germany), **1995**, Chapter 9, pp. 471–495.

[4] a) A.-M. Giroud-Godquin, P. M. Maitlis, *Angew. Chem.* **1991**, *103*, 370–398; *Angew. Chem. Int. Ed. Engl.* **1991**, *30*, 375–402; b) S. A. Hudson, P. M. Maitlis, *Chem. Rev.* **1993**, *93*, 861–885; c) D. W. Bruce, *J. Chem. Soc. Dalton Trans.* **1993**, 2983–2989; d) A.-M. Giroud-Godquin, *Coord. Chem. Rev.* **1998**, *178–180*, 1485; e) P. Espinet, *Gold Bull.* **1999**, *32*, 127–225.

[5] For a comprehensive review, see K. Binnemans, C. Görller-Walrand, *Chem. Rev.* **2002**, *102*, 2303–2346.

[6] H. Nozary, C. Piguet, P. Tissot, G. Bernardinelli, J.-C. G. Bünzli, R. Deschenaux, D. Guillon, *J. Am. Chem. Soc.* **1998**, *120*, 12274–12288.

[7] a) Y. Galyametdinov, M. A. Athanassopoulou, K. Griesar, O. Kharitonova, E. A. Soto Bustamante, L. Tinchurina, I. Ovchinnikov, W. Haase, *Chem. Mater.* **1996**, *8*, 922–926; b) K. Binnemans, Y. G. Galymetdinov, S. R. Collinson, D. W. Bruce, *J. Mater. Chem.* **1998**, *8*, 1551–1553; c) K. Binnemans, Y. G. Galyametdinov, R. Van Deun, D. W. Bruce, S. R. Collinson, A. P. Polishchuk, I. Bikchantaev, W. Haase, A. V. Prosvirin, L. Tinchurina, U. Litvinov, A. Gubajdullin, A. Rakhmatullin, K. Uytterhoeven, L. Van Meervelt, *J. Am. Chem. Soc.* **2000**, *122*, 4335–4344; d) R. Van Deun, K. Binnemans, *Liq. Cryst.* **2001**, *28*, 621–627; e) Y. Galyametdinov, W. Haase, L. Malykhina, A. Prosvirin, I. Bikchantaev, A. Rakhmatullin, K. Binnemans, *Chem. Eur. J.* **2001**, *7*, 99–105; f) K. Binnemans, D. Moors, T. N. Parac-Vogt, R. Van Deun, D. Hinz-Hübner, G. Meyer, *Liq. Cryst.* **2002**, *29*, 1209–1216.

[8] a) C. Piechocki, J. Simon, J. J. André, D. Guillon, P. Petit, A. Skoulios, P. Weber, *Chem. Phys. Lett.* **1985**, *122*, 124–128; b) H. Miwa, N. Kobayashi, K. Ban, K. Ohta, *Bull. Chem. Soc. Jpn.* **1999**, *72*, 2719–2728; c) K. Binnemans, J. Sleven, S. De Feyter, F. C. De Schryver, B. Donnio, D. Guillon, *Chem. Mater.* **2003**, *15*, 3930–3938.

[9] a) K. Binnemans, K. Lodewyckx, B. Donnio, D. Guillon, *Chem. Eur. J.* **2002**, *8*, 1101–1105; b) K. Binnemans, K. Lodewyckx, *Supramol. Chem.* **2003**, *15*, 485–494; c) E. Terazzi, J.-M. Bénech, J.-P. Rivera, G. Bernardinelli, B. Donnio, D. Guillon, C. Piguet, *Dalton Trans.* **2003**, 769–772; d) E. Terazzi, S. Torelli, G. Bernardinelli, J.-P. Rivera, J.-M. Bénech, C. Bourgogne, B. Donnio, D. Guillon, D. Imbert, J.-C. G. Bünzli, A. Pinto, D. Jeannerat, C. Piguet, *J. Am. Chem. Soc.* **2005**, *127*, 888–903; e) K. Binnemans, K. Lodewyckx, B. Donnio, D. Guillon, *Eur. J. Inorg. Chem.* **2005**, 1506–1513; f) K. Binnemans, K. Lodewyckx, T. Cardinaels, T. N. Parac-Vogt, C. Bourgogne, D. Guillon, B. Donnio, *Eur. J. Inorg. Chem.* **2006**, 150–157.

[10] a) T. Cardinaels, K. Driesen, T. N. Parac-Vogt, B. Heinrich, C. Bourgogne, D. Guillon, B. Donnio, K. Binnemans, *Chem. Mater.* **2005**, *17*, 6589–6598; b) E. Terazzi, B. Bocquet, S. Campidelli, B. Donnio, D. Guillon, R. Deschenaux, C. Piguet, *Chem. Commun.* **2006** 2922–2924.

[11] a) C. A. Hunter, J. K. M. Sanders, *J. Am. Chem. Soc.* **1990**, *112*, 5525–5534; b) C. A. Hunter, *Chem. Soc. Rev.* **1994**, *23*, 101–109; c) C. A. Hunter, K. R. Lawson, J. Perkins, C. J. Urch, *J. Chem. Soc. Perkin Trans. 2* **2001**, 651–669; d) S. L. Cockroft, C. A. Hunter, K. R. Lawson, J. Perkins, C. J. Urch, *J. Am. Chem. Soc.* **2005**, *127*, 8594–8595.

[12] a) J. P. Bedel, H. T. Nguyen, J. C. Rouillon, J. P. Marcerou, G. Sigaud, P. Barois, P. *Mol. Cryst. Liq. Cryst.* **1999**, *332*, 163–171; b) H. T. Nguyen, J. C. Rouillon, J. P. Marcerou, J. P. Bedel, P. Barois, S. Sarmento, *Mol. Cryst. Liq. Cryst.* **1999**, *328*, 177–184; c) J. P. Bedel, J. C. Rouillon, J. P. Marcerou, M. Laguerre, H. T. Nguyen, M. F. Achard, *Liq. Cryst.* **2000**, *27*, 1411–1421; d) J. P. Bedel, J. C. Rouillon, J. P. Marcerou, M. Laguerre, M. F. Achard, H. T. Nguyen, *Liq. Cryst.* **2000**, *27*, 103–113; e) J. P. Bedel, J. C. Rouillon, J. P. Marcerou, M. Laguerre, H. T. Nguyen, M. F. Achard, *Liq. Cryst.* **2001**, *28*, 1285–1292.

[13] J. J. Reczek, K. R. Villazor, T. M. Swager, B. L. Iverson, *J. Am. Chem. Soc.* **2006**, *128*, 7995–8002.

[14] a) R. Deschenaux, J.-L. Marendaz, J. Santiago, *Helv. Chim. Acta* **1993**, *76*, 865–876; b) K. E. Rowe, D. W. Bruce, *J. Mater. Chem.* **1998**, *8*, 331–341.

[15] J. H. Markgraf, B. Y. Choi, *Synth. Commun.* **1999**, *29*, 2405–2407.

[16] G. W. Kabalka, N. K. Reddy, C. Narayana, *Tetrahedron Lett.* **1993**, *34*, 7667–7668.

[17] F. H. Allen, O. Kennard, D. G. Watson, L. Brammer, A. G. Orpen, R. Taylor, *J. Chem. Soc. Perkin Trans. II* **1987**, S1-S19.

[18] U. C. Singh, P. A. Kollman, *J. Comput. Chem.* **1984**, *5*, 129–145.

[19] R. D. Shannon, *Acta Crystallogr. Sect. A* **1976**, *32*, 751–767.

[20] J.-C. G. Bünzli, B. Klein, G. Chapuis, K. J. Schenk, *Inorg. Chem.* **1982**, *21*, 808–812.

[21] a) H. Gampp, M. Maeder, C. J. Meyer, A. Zuberbühler, *Talanta* **1985**, *32*, 1133–1139; b) H. Gampp, M. Maeder, C. J. Meyer, A. Zuberbühler, *Talanta* **1986**, *33*, 943–951.

[22] E. Terazzi, J.-P. Rivera, N. Ouali, C. Piguet, *Magn. Reson. Chem.* **2006**, *44*, 539–552.

[23] H. Günther, *NMR Spectroscopy*, Wiley, Chichester, New York, **1980**, pp. 74–86.

[24] a) P. Stilbs, *Prog. Nucl. Magn. Reson. Spectrosc.* **1986**, *19*, 1–45; b) A. R. Waldeck, P. W. Kuchel, A. J. Lennon, B. E. Chapman, *Prog. Nucl. Magn. Reson. Spectrosc.* **1997**, *30*, 39–68; c) P. S. Pregosin, E. Martinez-Viviente, P. G. A. Kumar, *Dalton Trans.* **2003**, 4007–4014; d) P. S. Pregosin, P. G. P. G. A. Kumar, I. Fernandez, *Chem. Rev.* **2005**, *105*, 2977–2998.

[25] a) O. Kahn, *Adv. Inorg. Chem.* **1995**, *43*, 179–259; b) O. Kahn, *Molecular Magnetism*, VCH, Weinheim (Germany), **1993**, pp. 148–184; c) J.-M. Senegas, G. Bernardinelli, D. Imbert, J.-C. G. Bünzli, P.-Y. Morgantini, J. Weber, C. Piguet, *Inorg. Chem.* **2003**, *42*, 4680–4695;

d) J. Curély, B. Barbara, *Struct. Bonding (Berlin)* **2006**, *122*, 207–250.
[26] H. Nozary, C. Piguet, J.-P. Rivera, P. Tissot, P.-Y. Morgantini, J. Weber, G. Bernardinelli, J.-C. G. Bünzli, R. Deschenaux, B. Donnio, D. Guillon, *Chem. Mater.* **2002**, *14*, 1075–1090.
[27] J.-C. G. Bünzli, C. Piguet, *Chem. Rev.* **2002**, *102*, 1897–1928.
[28] W. T. Carnall, P. R. Fields, K. Rajnak, *J. Chem. Phys.* **1968**, *49*, 4443–4446.
[29] a) S. Tobita, M. Arakawa, I. Tanaka, *J. Phys. Chem.* **1984**, *88*, 2697–2702; b) S. Tobita, M. Arakawa, I. Tanaka, *J. Phys. Chem.* **1985**, *89*, 5649–5654.
[30] C. Piguet, A. F. Williams, G. Bernardinelli, E. Moret, J.-C. G. Bünzli, *Helv. Chim. Acta* **1992**, *75*, 1697–1717.
[31] a) K. Binnemans, L. Malykhina, V. S. Mironov, W. Haase, K. Driesen, R. Van Deun, L. Fluyt, C. Görller-Walrand, Y. G. Galyametdinov, *ChemPhysChem* **2001**, *2*, 680–683; b) K. Binnemans, D. Moors, *J. Mater. Chem.* **2002**, *12*, 3374–3376; c) S. Suarez, O. Mamula, D. Imbert, C. Piguet, J.-C. G. Bünzli, *Chem. Commun.* **2003**, 1226–1227; d) R. Van Deun, B. De Fré, D. Moors, K. Binnemans, *J. Mater. Chem.* **2003**, *13*, 1520–1522; e) E. Guillet, D. Imbert, R. Scopelliti, J.-C. G. Bünzli, *Chem. Mater.* **2004**, *16*, 4063–4070; f) S. Suarez, D. Imbert, F. Gumy, C. Piguet, J.-C. G. Bünzli, *Chem. Mater.* **2004**, *16*, 3257–3266; g) L. N. Puntus, K. J. Schenk, J.-C. G. Bünzli, *Eur. J. Inorg. Chem.* **2005**, 4739–4744.
[32] J.-C. G. Bünzli, E. Moret, J.-R. Yersin, *Helv. Chim. Acta* **1978**, *61*, 762.
[33] G. Schwarzenbach, *Complexometric Titrations*; Chapman & Hall, London, **1957**, p. 8.
[34] A. Altomare, M. C. Burla, M. Camalli, G. Cascarano, C. Giacovazzo, A. Guagliardi, G. Moliterni, G. Polidori, R. Spagna, *J. Appl. Crystallogr.* **1999**, *32*, 115.
[35] XTAL 3.2, User's Manual (Eds.: S. R. Hall, H. D. Flack, J. M. Stewart), Universities of Western Australia and Maryland, **1989**.
[36] C. K. Johnson, ORTEP II, Report ORNL-5138, Oak Ridge National Laboratory: Oak Ridge, Tennessee, **1976**.
[37] E. R. Malinowski, D. G. Howery, *Factor Analysis in Chemistry*, Wiley, New York, Chichester, **1980**.
[38] D. Wu, A. Chen, C. S. Johnson, Jr., *J. Magn. Reson. A* **1995**, *155*, 260.
[39] A.-S. Chauvin, F. Gumy, D. Imbert, J.-C. G. Bünzli, *Spectrosc. Lett.* **2004**, *37*, 517.
[40] A. D. Becke, *J. Chem. Phys.* **1993**, *98*, 5648.
[41] Gaussian 03, Revision B.03, M. J. Frisch, G. W. Trucks, H. B. Schlegel, G. E. Scuseria, M. A. Robb, J. R. Cheeseman, J. A. Montgomery, Jr., T. Vreven, K. N. Kudin, J. C. Burant, J. M. Millam, S. S. Iyengar, J. Tomasi, V. Barone, B. Mennucci, M. Cossi, G. Scalmani, N. Rega, G. A. Petersson, H. Nakatsuji, M. Hada, M. Ehara, K. Toyota, R. Fukuda, J. Hasegawa, M. Ishida, T. Nakajima, Y. Honda, O. Kitao, H. Nakai, M. Klene, X. Li, J. E. Knox, H. P. Hratchian, J. B. Cross, V. Bakken, C. Adamo, J. Jaramillo, R. Gomperts, R. E. Stratmann, O. Yazyev, A. J. Austin, R. Cammi, C. Pomelli, J. W. Ochterski, P.-Y. Ayala, K. Morokuma, G. A. Voth, P. Salvador, J. J. Dannenberg, V. G. Zakrzewski, S. Dapprich, A. D. Daniels, M. C. Strain, O. Farkas, D. K. Malick, A. D. Rabuck, K. Raghavachari, J. B. Foresman, J. V. Ortiz, Q. Cui, A. G. Baboul, S. Clifford, J. Cioslowski, B. B. Stefanov, G. Liu, A. Liashenko, P. Piskorz, I. Komaromi, R. L. Martin, D. J. Fox, T. Keith, M. A. Al-Laham, C. Y. Peng, A. Nanayakkara, M. Challacombe, P. M. W. Gill, B. Johnson, W. Chen, M. W. Wong, C. Gonzalez, J. Pople, J. A.; Gaussian, Inc., Wallingford CT, **2004**.
[42] N. Godbout, D. R. Salahub, J. Andzelm, E. Wimmer, *Can. J. Chem.* **1992**, *70*, 560.
[43] a) M. Dolg, H. Stoll, A. Savin, H. Preuss, *Theor. Chim. Acta* **1989**, *75*, 173; b) M. Dolg, H. Stoll, A. Savin, H. Preuss, *Theor. Chim. Acta* **1993**, *85*, 441.
[44] MOLEKEL 4.3, P. Flükiger, H. P. Lüthi, S. Portmann, J. Weber, Swiss Center for Scientific Computing, Manno (Switzerland), **2000–2002** (http://www.cscs.ch/molekel/).
[45] a) S. J. A. van Gisbergen, J. G. Snijders, E. J. Baerends, *Comput. Phys. Commun.* **1999** *118*, 119; b) A. Rosa, E. J. Baerends, S. J. A. van Gisbergen, E. van Lenthe, J. A. Groeneveld J. G. Snijders, *J. Am. Chem. Soc.* **1999**, *121*, 10356.
[46] ADF2005.01, SCM, Theoretical Chemistry, Vrije Universiteit, Amsterdam (The Netherlands), http://www.scm.com.
[47] E. van Lenthe, A. E. Ehlers, E. J. Baerends, *J. Chem. Phys.* **1999**, *110*, 8943.
[48] P. R. T. Schipper, O. V. Gritsenko, S. J. A. van Gisbergen, E. J. Baerends, *J. Chem. Phys.* **2000**, *112*, 1344.

Received: September 28, 2006
Published online: January 16, 2007

